Summer 2024

Assessing The Impact Of Spacecraft Fragmentation In The Cislunar Region

Marta Lopez Castro
Embry-Riddle Aeronautical University, lopezcam@my.erau.edu

ASSESSING THE IMPACT OF SPACECRAFT FRAGMENTATION IN THE CISLUNAR REGION

By

Marta López Castro

A Thesis Submitted to the Faculty of Embry-Riddle Aeronautical University

In Partial Fulfillment of the Requirements for the Degree of

Master of Science in Aerospace Engineering

July 2024

Embry-Riddle Aeronautical University

Daytona Beach, Florida

ASSESSING THE IMPACT OF SPACECRAFT FRAGMENTATION

IN THE CISLUNAR REGION

By

Marta López Castro

This Thesis was prepared under the direction of the candidate's Thesis Committee Chair, Dr. David Canales, Department of Aerospace Engineering, and has been approved by the members of the Thesis Committee. It was submitted to the Office of the Senior Vice President for Academic Affairs and Provost, and was accepted in the partial fulfillment of the requirements for the Degree of Master of Science in Aerospace Engineering.

THESIS COMMITTEE

Chair, Dr. David Canales	Member, Dr. Troy Henderson
Member, Dr. Hao Peng	
Graduate Program Coordinator, Dr. Hever Moncayo	Date
Dean of the College of Engineering, Dr. James W. Gregory	Date
Associate Provost of Academic Support, Dr. Kelly Austin	Date

A mi Familia, en especial a mi Abuelo Gonzalo, por enseñarme a despegar;
y a Javi, por hacerme volar cada día como si fuese la primera vez

To my Family, especially to my Grandpa Gonzalo, for encouraging me to spread my wings;
and to Javi, for making me fly every day as if it were the first time

ACKNOWLEDGMENTS

I would like to first thank my Family for all the support I have always received from them. To my parents, I have become who I am because of everything you have taught me. Thank you for all the freedom you've always given me and for helping me pursue my dreams, I will always be in debt to you. Also to my sister, thank you for always being there for your little you, you've always been a reference to me. Special thanks to Martín, Carmen, and Elena for keeping the little girl inside me alive. I hope I could be an example to follow your dreams, you have a whole world to discover.

The Dual Degree Program agreed between Universidad Europea de Madrid and Embry Riddle Aeronautical University has been a pleasure to me, and I would like to thank both Universities for letting me live this experience. I am deeply grateful to have been a member of the Space Trajectories and Applications Research Group led by my advisor, Dr. David Canales. Thank you for all the acknowledgment you provided me throughout this year and for the advice regarding planning and organization. I would also like to thank my committee members, Dr. Troy Henderson and Dr. Hao Peng for taking the time to collaborate with me and suggesting different ways to improve my research.

To my friends from Santiago and the ones from Madrid. You've always believed in me even when I was falling. Thank you for being there through thick and thin and for sharing life adventures. I would also like to thank all the people I met here. You have inspired me and I am sure you will achieve your milestones. I will miss you.

Last but not least, there are not enough words to express my gratitude for the support Javi has given me during this year. Distance has been a main character, but it has only brought us closer together. I'm very proud of you and I'm excited to start new stages together. Thank you for the special dates, for calling me every morning, and for our late-night conversations. You're my favorite life partner, my best friend, and the love of my life.

It is a privilege that I can count on all of you and I appreciate your support throughout my life. My achievements are also yours as you make them possible.

ABSTRACT

In the last decades, space missions have followed great advancements due to technological improvements and the extensive research developed in the field. Some of these missions are increasingly focusing on satellites orbiting the Moon. The Cislunar region is known to have a higher non-linear chaotic component in the dynamics compared to the low-Earth environment. This research is focused on studying the impact that a satellite explosion has in the Cislunar vicinity. The study is conducted for different periodic orbits that are key destinations for Cislunar traffic. By varying the initial conditions, simulations of explosions at different locations of the orbits are carried out and the debris propagation is analyzed. This research emphasizes the creation of a robust debris propagation scheme and the development of comprehensive databases to address the high computational costs associated with debris propagation. The goal of these simulations is to identify locations in the region where it would be more dangerous for an explosion to occur. Furthermore, it is possible to evaluate the potential hazard that the debris would entail to other satellites within the system. The understanding of these impacts will enhance safety measures, considering the risks and dangers associated with this environment and forecasting future needs and policies.

TABLE OF CONTENTS

LIST OF FIGURES

Figure **Page**

Figure **Page**

Figure **Page**

LIST OF TABLES

Table **Page**

NOMENCLATURE

$2BP$	Two-Body Problem
$[s_{exp}, t_{exp}]$	Fragments State Vector
ΔV	Ejection Velocity of the Explosion
μ	Mean
$\overline{r}_E$	Distance from the barycenter to the Earth
$\overline{r}_M$	Distance from the barycenter to the Moon
σ	Standard Deviation
A/M	Area-to-mass ratio of the fragments of an explosion
$BCR4BP$	Bicircular Restricted Four-Body Problem
$CR3BP$	Circular Restricted Three-Body Problem
DRO	Distant Retrograde Orbit
EOM	Equations of motion
GUI	Graphic User Interface
ICs	Initial Conditions
JC	Jacobi Constant
KE	Kinetic Energy
l^*	Characteristic Distance
L_1	First Lagrange Point
L_2	Second Lagrange Point

L_3	Third Lagrange Point
L_4	Fourth Lagrange Point
L_5	Fifth Lagrange Point
L_c	Particle Characteristic Length for the NASA SBM
M	Fragment Mass for the NASA SBM
m^*	Characteristic Mass
m_p	Particle Mass
$N(L_c)$	Number of Fragments
$NASA\ SBM$	NASA Standard Break-Up Model
$NRHO$	Near-Rectilinear Halo Orbit
R_{SoI}	Radius of the Sphere of Influence
$R_{Earth-SoI_{2BP}}$	Radius of the SoI of the Earth applying the $2BP$
$R_{Earth-SoI_{CR3BP}}$	Radius of the SoI of the Earth applying the $CR3BP$
$R_{Moon-SoI_{2BP}}$	Radius of the SoI of the Moon applying the $2BP$
$R_{Moon-SoI_{CR3BP}}$	Radius of the SoI of the Moon applying the $CR3BP$
s/c	Spacecraft
SoI	Sphere of Influence
t^*	Characteristic Time
U^*	Pseudo-potential function of the differential $CR3BP$ equations
ZVC	Zero Velocity Curve

μ^*	Mass ratio for the restricted three-body problem
A_x	Cross-Sectional Area of the Explosion Fragments
d_{SoI}	Gravitation Ratio
m_E	Mass of the Earth
m_M	Mass of the Moon
$r_{E-s/c}$	Distance from Earth to the spacecraft
$r_{M-s/c}$	Distance from Moon to the spacecraft
r_{E-M}	Distance from the Earth to the Moon

1 Introduction

Over the next twenty years, the Cislunar region is set to host over 50 missions with various payloads, highlighting its growing importance across scientific, commercial, and military sectors, key for expansion and investment [1–5]. The Cislunar region includes the spatial volume between the Earth and the Moon, separated by almost 400,000 km. This region is heavily influenced by the gravitational forces of both celestial bodies, resulting in highly nonlinear and more chaotic behavior than orbits close to Earth, making predicting the evolution of debris clouds through the system challenging. Debris poses a significant risk to missions, as even a single collision can result in catastrophic failure. Enhancing the understanding of these impacts will improve safety measures, considering the inherent risks and dangers of this environment.

1.1 Problem Scope and Definition

The concern over debris has been a focus of earlier studies. Previous works analyze the near-Earth environment, ensuring missions' safety around the Earth. Some studies use the two-body problem ($2BP$) [6] in which debris behavior differs from the dynamical model of interest, the circular restricted three-body problem ($CR3BP$) . Other researchers have studied fragmentation events near the Sun-Earth Lagrange Points [7], using the $CR3BP$ equations for the Sun-Earth system. Their findings indicate that approximately half of the fragments moved closer to the Earth, while the other half moved away from it. Other studies focus on Cislunar debris due to meteoroids [8, 9] and Kordylewski clouds [10, 11]. Although these issues are also important and a point to consider when planning a mission, it does not cover all the dangers in the region.

Other investigations study the evolution of space debris resulting from catastrophic mishaps close to the Earth-Moon Lagrange points. Additionally, these studies analyze the survivability of spacecraft in periodic orbits, applying perturbations such as the solar gravity, using the bicircular restricted four-body problem (BCR4BP) which is an extension of the $CR3BP$ that includes the influence of the solar gravity [10, 12–18]. Although the results from these studies are more precise, the higher computational cost limits the number of debris fragments that are considered.

Fragmentation events in the vicinity of L_2 Earth-Moon Lagrange point are studied for different

periodic orbits, such as near-rectilinear halo orbits (NRHO) , distant retrograde orbits (DRO) and Lyapunov orbits [1, 19, 20]. Black et al. simulate explosions for single and multiple fragmentation location cases studying fragment behavior based on energy levels and orbit locations near the L_2 Lagrange point.

As mentioned, different studies analyze the effects of explosions in such region, but the literature frequently overlooks the high computational cost of simulating fragmentation events. Due to limitations on debris generation, it is often difficult to obtain patterns of evolution and relationships between explosions in different orbits and regions. This research bridges that gap for better research development. Afterward, the impact on the Cislunar region is studied, with special interest in the libration points and the vicinity of the Moon.

1.2 Research Goal

The primary goal of this investigation is to enhance the assessment of the impacts of debris in the Cislunar region by creating a comprehensive database of debris generated from spacecraft explosions. This involves setting up detailed simulations of explosions in various Cislunar orbits to study their effects thoroughly. Special attention is given to libration point orbits and the vicinity of the Moon. The research also analyzes the potential impacts on other orbiting satellites to evaluate the viability and safety of future missions, considering the existing and predicted amounts of debris in the region.

1.3 Highlights

The key contributions of this work are summarized as follows:

- Efficient computation process for modeling explosions.
- Evaluation of different fragmentation models to determine the best fit for the Cislunar region.
- Creation of comprehensive databases for orbits, explosions, and debris to improve computational efficiency.
- Analysis of debris to identify danger zones and enhance safety measures.
- Examination of explosions in various orbital families to study debris evolution and orbital parameters.

- Development of a Graphical User Interface (GUI) to improve understanding and analysis of debris-related issues.

These highlights demonstrate the comprehensive approach taken to address the challenges of debris management in the Cislunar region.

1.4 Thesis Outline

Chapter 2 outlines the methodology used in this research. First, the dynamical model computed for the system, the circular restricted three-body problem ($CR3BP$), is described, including information related to periodic orbits and zero velocity curves ($ZVCs$) relevant to the Cislunar region and other parameters, e.g., the Jacobi Constant (JC) and Lagrange points. Boundaries of the system are specified by the sphere of influence (SoI) of the Moon and the Earth. Then, the fragmentation models studied are detailed, the NOAA 16 Battery Explosion Simulation, and the NASA Standard Break-Up Model (NASA SBM) , as well as a comparison of the parameters obtained in both methods. Chapter 3 presents the setup of the fragmentation event, specifying initial conditions (ICs) such as the position where explosions occur and the time of evaluation. It defines the process of the simulation to compute explosions and introduces the generation of the databases used, the ones for orbits, explosions, and debris. Chapter 4 analyzes the results obtained for explosions occurring to s/c orbiting L_1 and L_2 Lyapunov orbits, compares explosions of those family orbits, and other simulations are computed for direct retrograde orbits (DROs) studying patterns due to the influence of the stability of the orbits. Furthermore, a section is included to validate the results obtained using the CR3BP model by comparing them with those from a higher-fidelity model. Chapter 5 analyzes the effect of debris on an orbiting satellite, presenting various cases of study regarding L_1 and L_2 Lyapunov orbits. Chapter 6 concludes the research by discussing the goals achieved and summarizing the future work considered necessary to continue investigating this field.

2 Methodology

This section outlines important concepts related to the methodology used for the computation of this research. The circular restricted three-body problem ($CR3BP$) is defined as the dynamical model applied to the study. Two fragmentation models are discussed and compared: the NOAA 16 battery explosion simulation and the NASA Standard Break-Up Model, both applied to collisions and explosions.

2.1 Dynamical Model – The Circular Restricted Three-Body Problem

The $CR3BP$ is a simplified dynamical model useful to describe the motion of a spacecraft under the influence of two primaries, one larger than the other [21]. More specifically, in the Cislunar region, the Earth and the Moon are the larger smaller primaries, respectively. It is considered that the two primary bodies move under the action of their gravitational accelerations [22]. The spacecraft is the third body of the problem and its mass is negligible as it is significantly smaller compared to the primaries. In this way, the barycenter of the primaries corresponds to the center of mass of the system, and the total mass of the system is defined as $m^* = m_E + m_M$. Based on the center of mass, a barycentric rotating frame is defined, where the $\hat{x}$-axis is directed from the Earth-Moon barycenter to the Moon, and the $\hat{z}$-axis is directed from the barycenter in the direction of the angular momentum vector of the system. A schematic model of the Earth-Moon $CR3BP$ is presented in Figure 2.1, depicting the three bodies and the Lagrange points within the barycentric rotating frame.

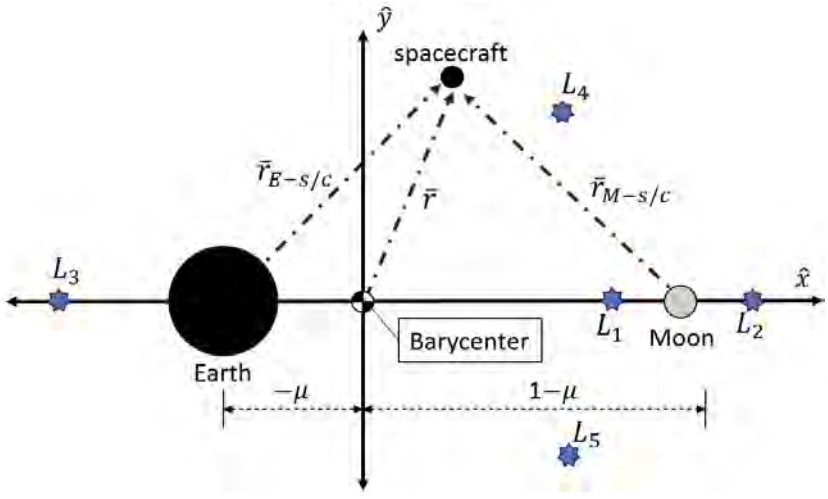

Figure 2.1 $CR3BP$ model in the Earth-Moon barycentric rotating frame

2.1.1 Equations of Motion

A dimensionless system of differential equations is implemented in the $CR3BP$. In order to nondimensionalize the problem, some characteristic values are defined [23]. The values used are included in Table 2.1 with a star exponent that denotes dimensionless.

Table 2.1 Characteristic parameters that define the Earth-Moon $CR3BP$

Parameter	**Definition**	**Value**
Distance	Earth-Moon distance	$l^* = 384,400$ km
Mass	Sum of Earth and Moon masses	$m^* = 6.0477 \cdot 10^{24}$ kg
Time	Time for the Moon to travel one radian around Earth	$t^* = 4.3425$ days
Mass ratio	Proportion of the Moon mass	$\mu^* = 1.2155 \cdot 10^{-2}$

The mass ratio is defined as relating the masses of the primaries as $\mu^* = m_M/(m_E + m_M)$, which helps to normalize the problem [21]. Earth and Moon's positions are defined in terms of the mass ratio, as $\overline{r}_E = [-\mu^*, 0, 0]^T$ and $\overline{r}_M = [1 - \mu^*, 0, 0]^T$, respectively. Finally, the characteristic time guarantees the dimensionless of the mean motion of the primaries to be equal to unity ($\omega^* = \omega t^* = 1$).

The equations of motion (EOM) that govern the evolution of the third body, depending on the derivatives with respect to dimensionless time represented by dots, are:

$$\ddot{x} - 2\dot{y} = \frac{\partial U^*}{\partial x} \tag{1}$$

$$\ddot{y} + 2\dot{x} = \frac{\partial U^*}{\partial y} \tag{2}$$

$$\ddot{z} = \frac{\partial U^*}{\partial z} \tag{3}$$

The EOM also depend on the pseudo-potential function of the differential equations system, U^*, given by:

$$U^* = \frac{1 - \mu^*}{r_{E-s/c}} + \frac{\mu^*}{r_{M-s/c}} + \frac{1}{2}(x^2 + y^2) \tag{4}$$

where $r_{E-s/c}$ and $r_{M-s/c}$ represent the distances from the Earth and the Moon to the spacecraft, respectively. The state vector in the $CR3BP$, $\bar{s}$, is defined to include three components of position and velocity.

2.1.2 Lagrange Points

There are other variables of interest for the $CR3BP$ model, such as the Lagrange points, also known as libration points. Their locations represent the regions of space where the s/c has zero velocity and acceleration [22], remaining stationary with respect to the Earth and the Moon. The Lagrange points are the equilibrium solutions for derivatives equal to zero:

$$\dot{x} = \dot{y} = \dot{z} = 0 \qquad \text{and} \qquad \ddot{x} = \ddot{y} = \ddot{z} = 0 \tag{5}$$

By substituting these values into Equations 1, 2 and 3, the equilibrium solutions are calculated by the following expressions [21]:

$$x - \frac{(1-\mu^*)(x+\mu^*)}{r_1^3} - \frac{\mu^*(x-1+\mu^*)}{r_2^3} = 0 \tag{6}$$

$$y\left(1 - \frac{1-\mu^*}{r_1^3} - \frac{\mu^*}{r_2^3}\right) = 0 \tag{7}$$

Note that the equilibrium points lie in the orbital plane, $z = 0$. The first three collinear solutions of the system are obtained by setting $y = 0$ and interpolating. Two triangular solutions correspond to L_4 and L_5 equilateral points, whose solutions lie 60º ahead of the Earth and the Moon. The solutions are included in Table 2.2 [22], and represented in the diagram of Figure 2.1:

Table 2.2 Solutions of the Lagrange Points

Lagrange Point	**Coordinates (nondim)**	**Coordinates (km)**
L_1	$[0.837, 0, 0]$	$[3.217 \cdot 10^5, 0, 0]$
L_2	$[1.156, 0, 0]$	$[4.444 \cdot 10^5, 0, 0]$
L_3	$[-1.005, 0, 0]$	$[-3.863 \cdot 10^5, 0, 0]$
L_4	$[0.5, 0.866, 0]$	$[1.922 \cdot 10^5, 3.329 \cdot 10^5, 0]$
L_5	$[0.5, -0.866, 0]$	$[1.922 \cdot 10^5, -3.329 \cdot 10^5, 0]$

2.1.3 Jacobi Constant

The Jacobi Constant, JC, is the only scalar integral for the system, defined as:

$$JC = 2U^* - (\dot{x}^2 + \dot{y}^2 + \dot{z}^2) \tag{8}$$

It gives information about the spacecraft's energy.

2.1.4 Zero Velocity Curves

A spacecraft zero velocity curve (ZVC) defines the boundaries of permissible motion in the system [21]. The $ZVCs$ depend on the value of the JC and are obtained by setting the velocity to zero in Equation 8, obtaining:

$$JC = 2U^* = \frac{1-\mu^*}{r_{E-s/c}} + \frac{\mu^*}{r_{M-s/c}} + \frac{1}{2}(x^2+y^2) \tag{9}$$

The coordinates that yield the same JC value form a surface bounded by the corresponding ZVC for that JC. Some ZVC examples are plotted in Figure 2.2 for the Earth-Moon system. As the value of the JC decreases, the forbidden surfaces shrink, resulting in a more chaotic system due to the reduced constraints in motion.

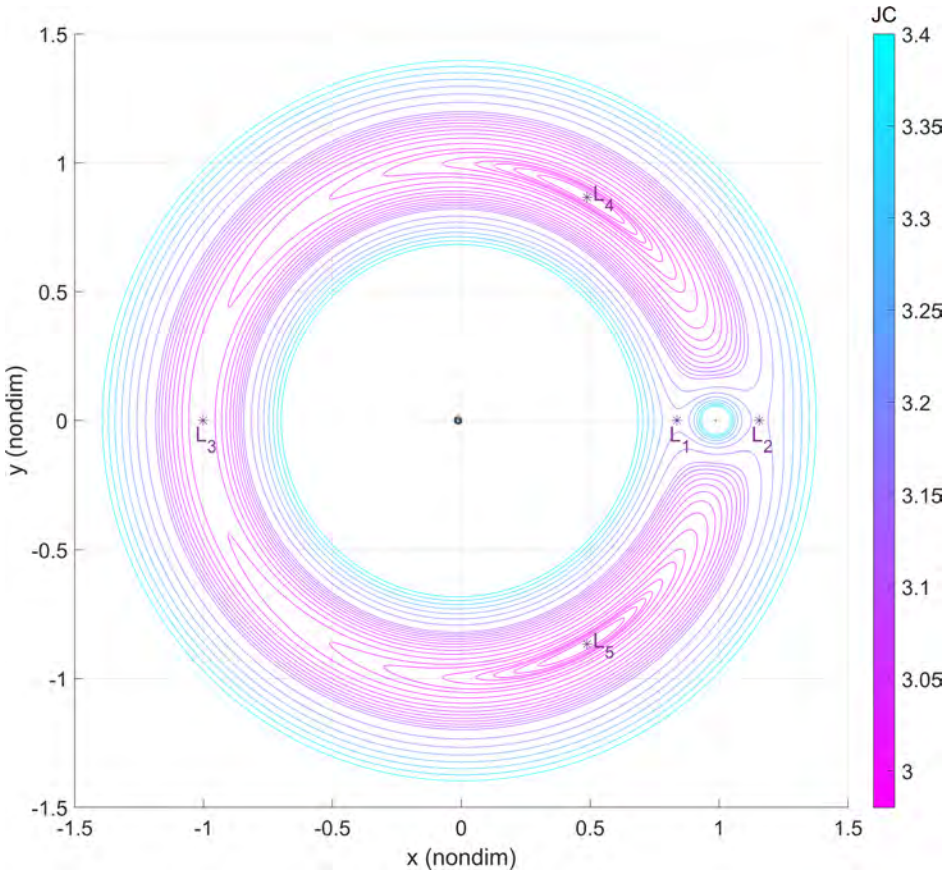

Figure 2.2 $ZVCs$ for different JC in the Earth-Moon $CR3BP$ system

2.1.5 Periodic Orbits

The motion around the Lagrange points may be categorized by families of periodic orbits, including Lyapunov, DROs, and NRHOs. Due to the highly nonlinear dynamics, with dynamics being much more variable in the Cislunar region compared to the near-Earth environment [24], some periodic orbit families possess characteristics not related to the $2BP$. Some of these orbits look similar to other two-body orbits but are perturbed by the second primary [21], i.e., the Moon. The member orbits of each family in the $CR3BP$ are defined by their period, stability, or Jacobi constant. The study focuses on Lyapunov orbits, although the interface is created such that debris propagation is obtained from any other families. Results are presented for orbits of the Lyapunov families around the Lagrange Points L_1 and L_2, as well as for DROs, due to their respective instabilities and stabilities in the Cislunar region. These orbits were selected to analyze patterns in debris scattering influenced by the stability of the orbit.

The DRO family consists of two-dimensional periodic orbits and bifurcates to 3D, obtaining the 3D DRO. This family includes orbits that pass near the Earth and the far side of the Moon, and others with close passages to L_1 and L_2 [24] (Figure 2.3).

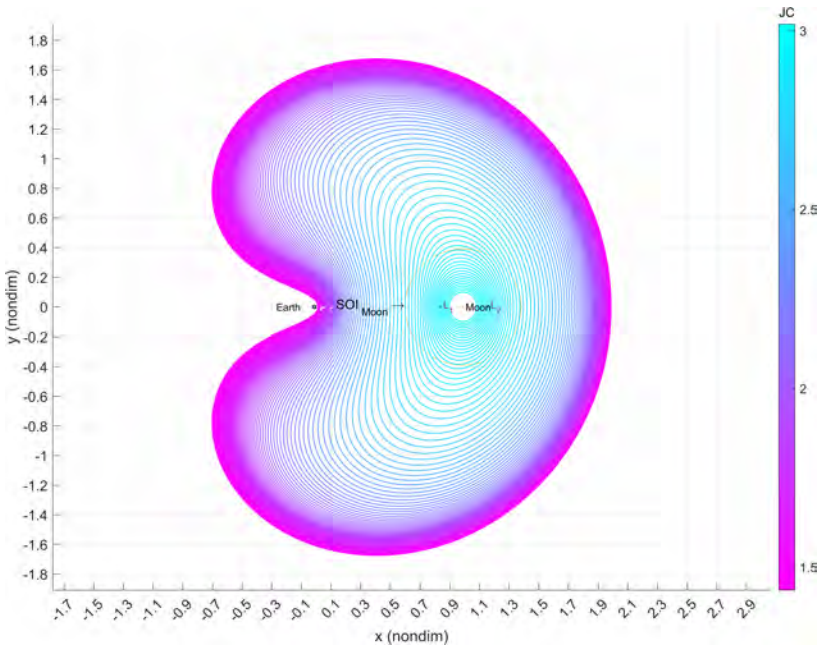

Figure 2.3 Distant Retrograde Orbit Family

The Lyapunov is a planar periodic orbit family that originates in the vicinity of each Lagrange point. For the cases of study, the L_1 and L_2 Lyapunov orbits cover the Cislunar region and present a close Lunar passage that is of interest when analyzing explosions of orbiting spacecraft [24]. Figures 2.4 and 2.5 represent the L_1 and L_2 families of Lyapunov orbits. For the simulations conducted in this research, only the Lyapunov orbits entirely within the SoI of the Moon are selected.

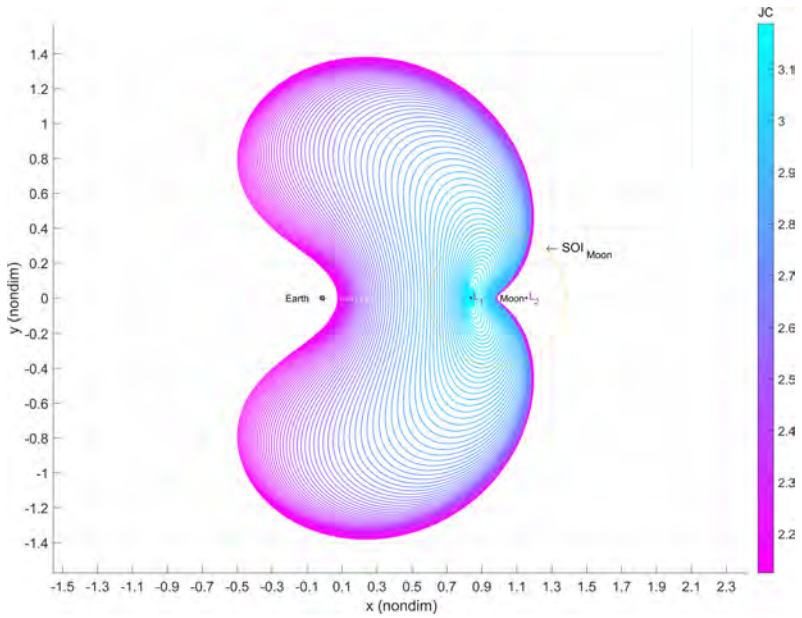

Figure 2.4 L_1 Lyapunov orbit family

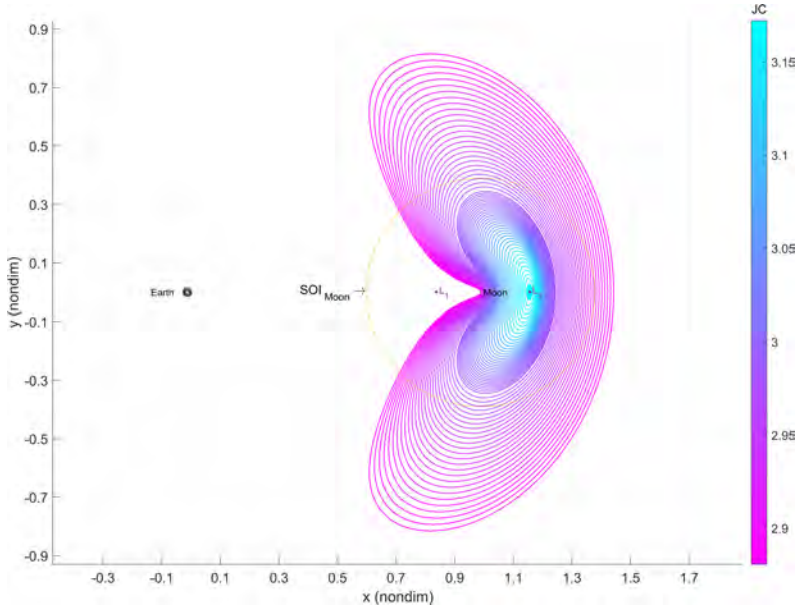

Figure 2.5 L_2 Lyapunov orbit family

2.1.6 Spheres of Influence of the primary bodies

The fragmentation events are configured in a system bounded inside the SoI of the Earth. When obtaining results, conclusions are made depending on the type of debris for each fragment. Debris is neglected if it escapes the system, which is defined by the sphere of influence of the Earth. As the research focuses on lunar orbits, the sphere of influence of the Moon is also interesting to observe the amount of debris orbiting in the region.

The classical radius of the SoI is calculated for the two-body problem ($2BP$) by the equation that relates the masses of the two bodies and their distance from each other, which for the case of the SoI of the Moon is defined as:

$$R_{SoI} = r_{E-M} \left(\frac{m_M}{m_E} \right)^{2/5} \tag{10}$$

However, the radius of these spheres is quite small for the $CR3BP$ system. Periodic orbits in the vicinity of L_1 and L_2 libration points are not included in the classical sphere of influence of the Moon. To improve that, a new value for the radius is obtained depending on the influence of the gravitational acceleration of the bodies.

It is selected a radius depending on the gravitation ratio, d_{SoI} . The value of the radius is selected by the distance to the Moon where d_SoI is equal to a certain small quantity [23].

This leads to a case-by-case design:

- *Sphere of Influence of the Moon*. Applied to the Earth-Moon $CR3BP$, the gravitational influence along the $\hat{x}$-axis is represented in Figure 2.6a. Comparing the new value with the classical, it is obtained:

$$R_{Moon-SoI_{2BP}} = 0.1720 \approx 66,100 \text{ km} \tag{11}$$

$$R_{Moon-SoI_{CR3BP}} = 0.3902 \approx 150,000 \text{ km} \tag{12}$$

- *Sphere of Influence of the Earth*. It is designed in the Sun-Earth $CR3BP$, which changes the characteristic values for the nondimensionalized parameters, e.g., the characteristic length is defined by the distance of the Earth to the Sun, $l^* = 1.5 \cdot 10^9$ km. As mentioned, the Sphere

of Influence of the Earth includes the whole system of this research, which means that debris out of the system is outside this sphere. However, the new Sphere of Influence of the Earth is very large for the Earth-Moon system, as it is 35 times the distance between the Earth and the Moon. Thus, the classical value is used for the analysis of the results. Figure 2.6b presents the gravitational influence of the Sun and the Earth, and the comparison of the radius for the case of study of a periodic orbit in the Sun-Earth $CR3BP$ in the vicinity of their L_1 and L_2 Lagrange Points, and it is shown the comparison of the classical and the new value.

$$R_{Earth-SoI_{2BP}} = 0.0062 \approx 924,000 \text{ km} \tag{13}$$

$$R_{Earth-SoI_{CR3BP}} = 0.0912 \approx 1.368 \cdot 10^7 \text{ km} \tag{14}$$

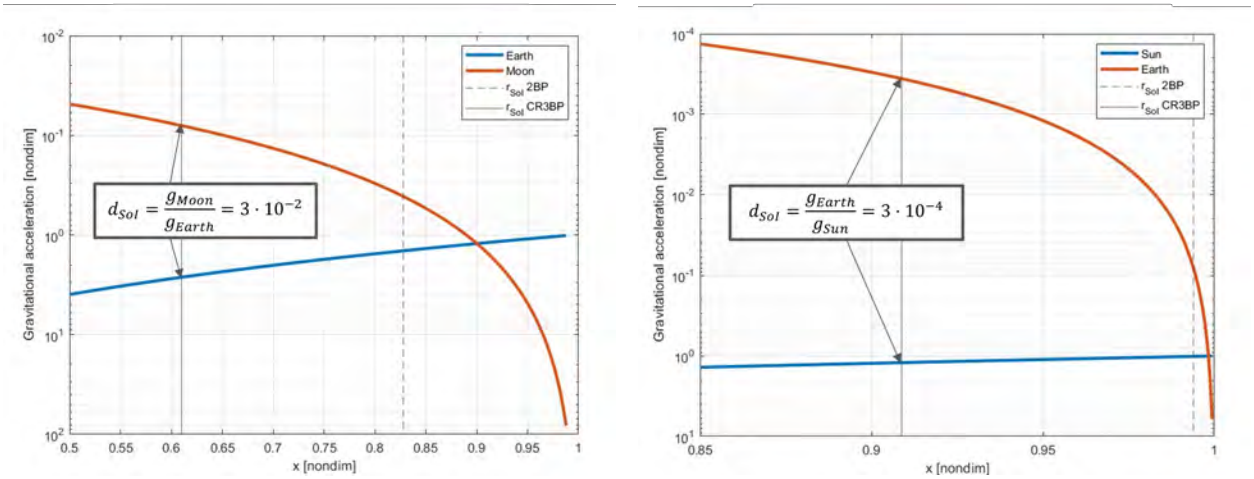

(a) Earth and Moon *(b)* Sun and Earth

Figure 2.6 Gravitational influence due to the two bodies along the $\hat{x}$-axis

2.2 Fragmentation Model

A fragmentation model defines a breakup event through statistical distributions for a given parameter. The main parameters to compute these events are the area-to-mass ratio, size, and velocity of each fragment after an explosion or collision [25]. There are various fragmentation models to generate fragmentation events based on these parameters. In this research, two of them are used to create explosions: the NASA Standard Break-Up Model [25] and the NOAA 16 simulation [12].

2.2.1 NOAA 16 Satellite Battery Explosion

This break-up model simulates the catastrophic mishap of the NOAA 16 satellite caused by a battery explosion [26]. Two parameters define the model: the mass distribution of the fragments and their ejection velocity after the explosion. A total of 135 satellite fragments are tracked to calculate a statistical distribution that fits the observed masses [12]. Therefore, the mass distribution in the model is represented by the resulting lognormal distribution with specified mean and standard deviation values:

$$\mu = -1.7286 \qquad \text{and} \qquad \sigma = 1.4511 \tag{15}$$

This lognormal distribution is configured so that the total mass of the fragments matches the initial mass of the spacecraft before the fragmentation event, with the distribution being random for each simulation.

The scalar value of the change in velocity depends on the mass of each fragment and is calculated based on the kinetic energy of the fragments. The relative velocities of the 135 debris particles tracked are used to calculate the relative kinetic energy of all fragments, obtaining an average of 6678 J [12]. The ejection velocity is modeled by assuming that all the fragments are imparted with this kinetic energy, following the relation defined as:

$$\Delta V = \sqrt{\frac{2 \cdot KE}{m_p}} = \sqrt{\frac{2 \cdot 6678}{m_p}} \tag{16}$$

where m_p is the mass of each particle and KE is the kinetic energy.

The mass and velocity distributions applied to a random simulation are plotted in Figure 2.7. To define the velocity vector, a random direction is assigned to the scalar values already calculated[27], obtaining omni-directional velocity distributions.

Computation process of NOAA 16 Break-Up Model

The procedure to compute the fragmentation model related to the NOAA 16 satellite battery explosion is described in the flowchart presented in Figure 2.8. The mass of the spacecraft is the input of the model, m_sat. By applying a lognormal distribution based on the observed explosion

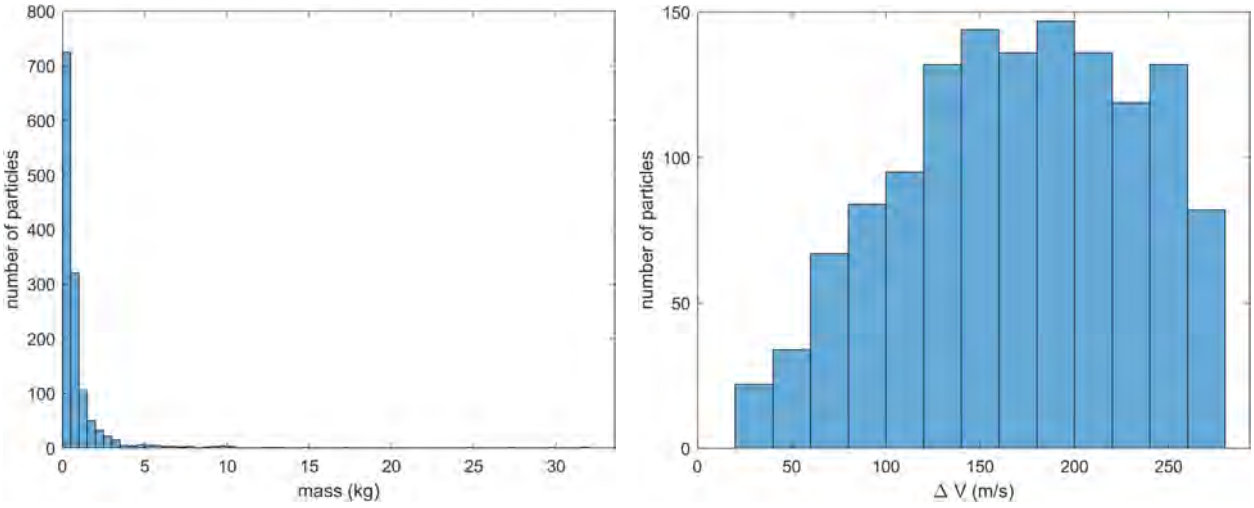

(a) Mass distribution of the fragments *(b)* Change in velocity distribution

Figure 2.7 NOAA 16 Model distributions

of the NOAA 16 satellite, the mass of each fragment, m_p, is calculated iteratively until their total mass equals the mass of the entire spacecraft. It is added a restriction to consider the values above the boundary defined by a minimum volume, Vol_{min} and minimum fragment length, $L_{c_{min}}$, considering the material density of the material, ρ. The change in velocity is calculated first as a scalar value and then a random direction is computed. The energy equation defined in Equation 16 depends on the value of kinetic energy to obtain the scalar value of the ejection velocity, $|\Delta V|$. The *direction* is defined by a uniform distribution, obtaining the velocity vector of each fragment, $\overline{\Delta V}$ as the output of the fragmentation model, as well as the number of total fragments generated, N_{tot}.

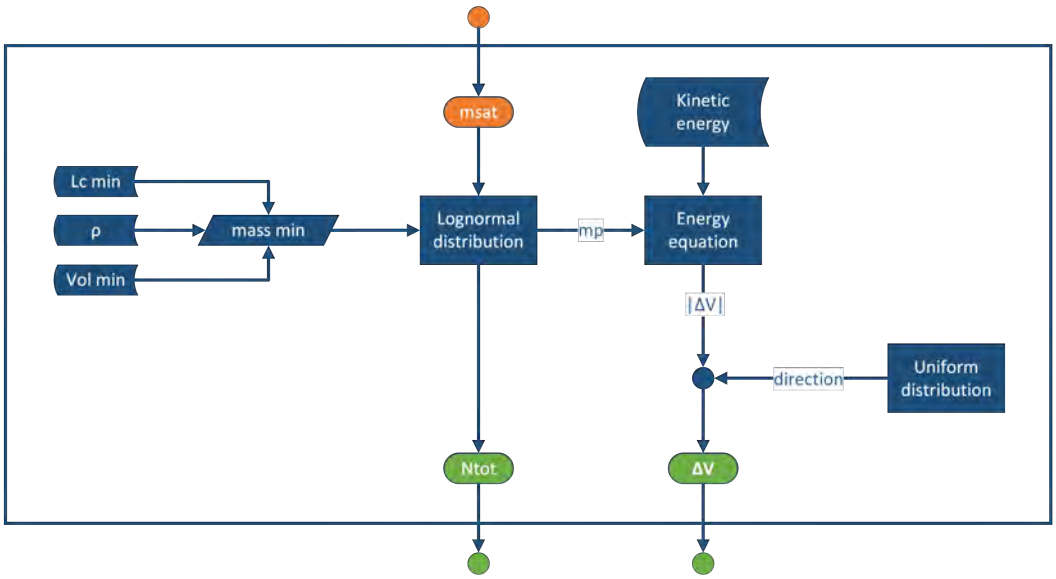

Figure 2.8 Flowchart of the computation of NOAA 16 Break-Up Model

2.2.2 The NASA Standard Break-Up Model

The definition of a break-up model has also been used by NASA to generate debris clouds. The NASA Standard Break-Up Model was originally created in the 1970s. Over the years, it has improved and some conditions have changed to achieve higher fidelity on the databases created, being the EVOLVE 4.0 the most recent model [25]. The input of this break-up model is the particle characteristic length, L_c , which represents the size of the fragments generated. Note that this parameter is different from the characteristic distance, l^*, defined for the $CR3BP$ system. The amount of particles is roughly based on the particle characteristic length, although the characteristics of each particle, i.e., the mass and ejection velocity, are random along statistical distributions [25].

The NASA SBM is a statistical model based on empirical data from different fragmentation events and the observation of the resultant debris [17]. The detection systems of debris that are taken into account in this model are generally effective for fragments with a minimum size of 10 cm [25]. For this reason, parameters are better defined for particles of this magnitude order, conducting this study for spacecraft explosions with a fragment characteristic length of 11 cm.

This method classifies the fragmentation whether it is catastrophic or non-catastrophic [28], considering that the break-up is catastrophic when the fragments exceed a specific energy level of 40 J/g. Taking this into account, explosions are considered catastrophic events, while some collisions are considered non-catastrophic. The mass distribution function to obtain the area-to-mass ratio, A/M, of the fragments generated is presented:

$$D_{A/M}^{s/c}(\lambda_c, \chi) = \alpha^{s/c}(\lambda_c) N(\mu_1^{s/c}(\lambda_c), \sigma_1^{s/c}(\lambda_c), \chi) + (1 - \alpha^{s/c}(\lambda_c)) N(\mu_2^{s/c}(\lambda_c), \sigma_2^{s/c}(\lambda_c), \chi) \quad (17)$$

where,

$$\lambda_c = \log_{10}(L_c) \quad (18)$$

$$\chi = \log_{10}(A/M) \quad (19)$$

$$N(\mu, \sigma, \chi) = \frac{1}{\sigma\sqrt{2\pi}} e^{-(\chi-\mu)^2/2\sigma^2} \quad (20)$$

Note that the process to obtain results in terms of mass is the same for both catastrophic and non-

catastrophic events, i.e., explosions and collisions. The statistical parameters of the distribution depend on the value of the characteristic length. Johnson et al. [25] details the boundary conditions for each one:

$$\alpha^{s/c} = \begin{cases} 0 & \lambda_c \leq -1.95 \\ 0.3 + 0.4(\lambda_c + 1.2) & -1.95 < \lambda_c < 0.55 \\ 1 & 0.55 \leq \lambda_c \end{cases} \tag{21}$$

$$\sigma_1^{s/c} = \begin{cases} 0.1 & \lambda_c \leq -1.3 \\ 0.1 + 0.2(\lambda_c + 1.3) & -1.3 < \lambda_c < -0.3 \\ 0.3 & -0.3 \leq \lambda_c \end{cases} \tag{22}$$

$$\sigma_2^{s/c} = \begin{cases} 0.5 & \lambda_c \leq -0.5 \\ 0.5 - (\lambda_c + 0.5) & -0.5 < \lambda_c < -0.3 \\ 0.3 & -0.3 \leq \lambda_c \end{cases} \tag{23}$$

$$\mu_1^{s/c} = \begin{cases} -0.6 & \lambda_c \leq -1.1 \\ -0.6 - 0.318(\lambda_c + 1.1) & -1.1 < \lambda_c < 0 \\ -0.95 & 0 \leq \lambda_c \end{cases} \tag{24}$$

$$\mu_2^{s/c} = \begin{cases} -1.2 & \lambda_c \leq -0.7 \\ -1.2 - 1.333(\lambda_c + 0.7) & -0.7 < \lambda_c < -0.1 \\ -2 & -0.1 \leq \lambda_c \end{cases} \tag{25}$$

The mass of the fragments is obtained by relating the cross-sectional area, A_x, to the area-to-mass ratio calculated with Equation 17:

$$M = \frac{A_x}{A/M} \tag{26}$$

A_x depends on the value of the fragment's characteristic length:

$$A_x = 0.540424 L_c^2 \qquad L_c < 0.167cm \tag{27}$$

$$A_x = 0.556945 L_c^{2.0047077} \qquad L_c \geq 0.167cm \tag{28}$$

The equations that define the collision model are briefly introduced for the calculation of the number of fragments and the changes in velocity. For explosions, general equations are presented and then applied specifically to the context of this research.

Collisions

Collisions are classified as catastrophic or non-catastrophic, depending on the relation between the relative kinetic energy of the smaller body and the mass of the larger one [25]. Catastrophic collisions lead to the fragmentation of both bodies. In the case of non-catastrophic events, only the smaller spacecraft is completely fragmented. The determination of the number of fragments, N, generated after a collision follows a power law distribution that depends on the characteristic length defined for the fragments, L_c:

$$N(L_c) = 0.1(M_{tot})^{0.75} L_c^{-1.71} \tag{29}$$

where the total mass is defined depending on whether the event is catastrophic or non-catastrophic [28]:

- For catastrophic events, the total mass is defined as the sum of the target (the larger object) and the projectile (the smaller object), in kg:

$$M_{tot} = m_{target} + m_{projectile} \tag{30}$$

- For non-catastrophic events, the total mass depends on the mass of the smaller body, in kg, and the collision velocity, expressed in km/s:

$$M_{tot} = m_{projectile} + m_{projectile} \times V^2 \tag{31}$$

The ejection velocity of the collision fragments is determined by the following distribution function:

$$D_{\Delta V}^{coll}(\chi, \nu) = N(\mu^{coll}(\chi), \sigma^{coll}(\chi), \nu) \tag{32}$$

where

$$\chi = \log_{10}(A/M) \tag{33}$$

$$\nu = \log_{10}(\Delta V) \tag{34}$$

$$\mu^{coll} = 0.9\chi + 2.9 \tag{35}$$

$$\sigma^{coll} = 0.4 \tag{36}$$

The parameters mentioned above are sufficient to define a fragmentation event caused by the collision of two bodies.

Explosions

To proceed with the creation of the explosion, first, it is required to select the particle characteristic length of study, L_c, that represents the size of the fragments generated. As mentioned above, this research is focused on $L_c = 11$ cm.

Next, the number of fragments generated for the specific L_c after an explosion is calculated:

$$N(L_c) = 6L_c^{-1.6} \tag{37}$$

The area-to-mass distribution is calculated from the initial characteristic length. The variables of the distribution are $\lambda_c = \log_{10}(L_c)$ and $\chi = \log_{10}(A/M)$, as shown in Equation 17. For the case applied to this study ($L_c = 11$ cm):

$$\alpha^{s/c} = 0.3966; \quad \mu_1^{s/c} = -0.645; \quad \sigma_1^{s/c} = 0.1683; \quad \mu_2^{s/c} = -1.2; \quad \sigma_2^{s/c} = 0.5 \tag{38}$$

The cross-sectional area A_x computed for the specific L_c follows the relation established in Equation 28 for $L_c \geq 0.167$cm where $A_x = 0.556945L_c^{2.0047077}$. The aforementioned parameters are substituted in Equation 26 obtaining the mass conversion of each fragment. The distribution of the change in velocity that follows each particle is calculated with:

$$D_{\Delta V}^{exp}(\chi, \nu) = N(\mu^{exp}(\chi), \sigma^{exp}(\chi), \nu) \tag{39}$$

where χ and ν are the ones defined in Equations 33 and 34. Additionally,

$$\mu^{exp} = 0.2\chi + 1.85 \tag{40}$$

$$\sigma^{exp} = 0.4 \tag{41}$$

The implementation of the NASA Break-Up Model generates a random number of fragments that correspond to a smaller mass compared to the initial mass of the spacecraft before the explosion. To assure mass conservation, a correction needs to be applied by adding a maximum of 20 fragments with larger characteristic lengths in a range of $L_{c_0} = 1$ and $L_{c_1} = 5$. These bigger particles simulate spacecraft components that are not destroyed during the explosion [17], such as pressurant tanks or nozzle bells. The λ parameter that depends on the particle characteristic length is obtained by the following distribution:

$$\lambda = -\frac{1}{\beta}\log_{10}(10^{-\beta\lambda_0} - P_\lambda(10^{-\beta\lambda_0} - 10^{-\beta\lambda_1})) \tag{42}$$

where, P_λ is a random variable uniformly distributed between 0 and 1, β is a constant equal to 1.6, and L_{c_0} and L_{c_1} are the lower and upper boundaries of the fragments characteristic length, respectively, that the defines the values of λ_0 and λ_1:

$$\lambda = \log_{10}(L_c) \quad \lambda_0 = \log_{10}(L_{c_0}) \quad \lambda_1 = \log_{10}(L_{c_1}) \tag{43}$$

The λ obtained when applying the distribution indicated in Equation 42 is used to identify the characteristic length of the bigger fragments. By computing the new L_c in Equations 37, 17 and 39, the velocity and mass are calculated. It is iteratively computed until the total mass of all the fragments equals the mass of the entire spacecraft, with a maximum number of additional fragments of 20. For example, in the case of $L_c = 11$ cm, the NASA expression in Equation 37 gives a solution of 206 fragments. By mass conservation, the total number of fragments is between 207 and 226. Figure 2.9 represents the statistical distributions applied for this specific characteristic length.

Computation process of NASA SBM

Figure 2.10 illustrates the computation process for the NASA SBM. Two inputs are required to start the simulation: the particle characteristic length, L_c, and the total mass of the satellite, m_{sat}. The characteristic length is used to determine the number of fragments, $N(L_c)$, as well as the cross-sectional area, A_x. The number of fragments is normally distributed to obtain the area-to-mass ratio, A/M. First, A/M is related to obtain the mass of each fragment: M. A random number of larger particles, *N([1m,5m])*, is used to ensure mass conservation, obtaining the original

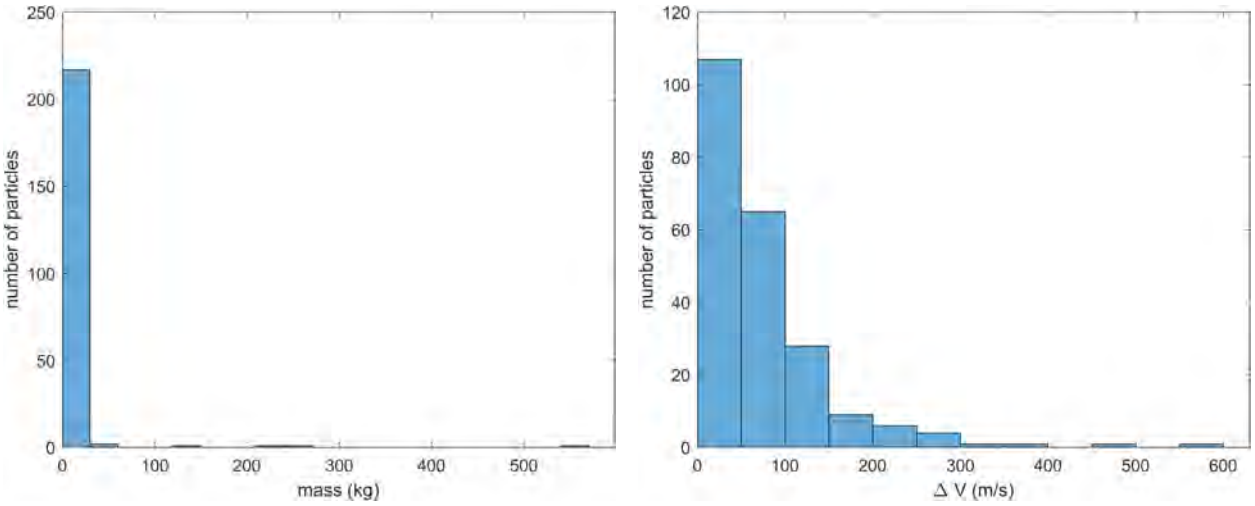

(a) Mass distribution of the fragments *(b)* Change in velocity distribution

Figure 2.9 NASA Standard Break-Up Model distributions for $L_c = 11$ cm

m_{sat}. Subsequently, the total number of fragments, N_{tot}, is calculated. Lastly, the selected L_c and A/M are used in a normal distribution to determine the scalar value of the ejection velocity for each particle, $|\Delta V|$. The *direction* of the velocities is determined using a uniform distribution, resulting in the ejection velocity vectors, $\overline{\Delta V}$. The outputs of the break-up model are both $\overline{\Delta V}$ and N_{tot}.

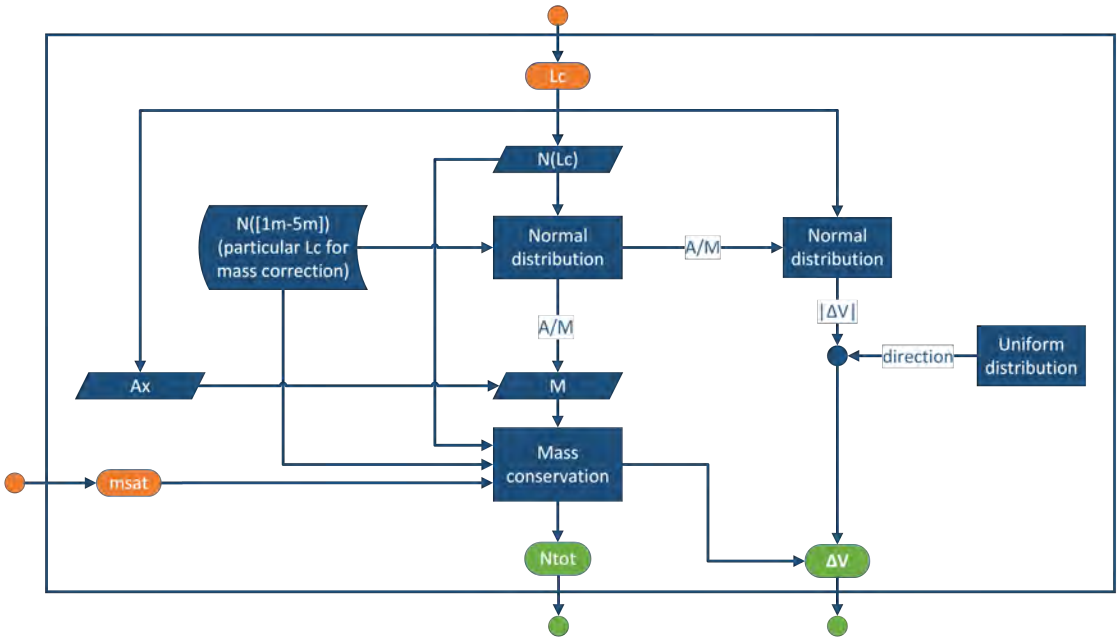

Figure 2.10 Flowchart of the computation of NASA SBM

2.2.3 Comparison of Methods

The results obtained for the parameters that define the explosions differ for each break-up model, as plotted in Figures 2.11 and 2.12. When examining the mass distribution in Figure 2.11a, the NOAA 16 simulation produces more fragments with a greater variance in masses compared to the NASA SBM. Specifically, the NASA SBM generates mostly smaller masses, under 0.1 kg, except for a few larger fragments added during the mass correction process. Additionally, it is important to note that generating more fragments increases the computational cost of simulating one or more explosions, which imposes limitations on the precision of the simulation results.

Regarding the ejection velocity of each fragment (Figures 2.11b and 2.12), the NOAA 16 model shows a broader dispersion in velocities, corresponding to the varied fragment masses. The average scalar velocity is high, which contributes to a more chaotic system as the Jacobi constant of the particles decreases. This fact presents challenges for the propagation computed using the $CR3BP$ dynamical model. In contrast, the NASA SBM results in lower velocities, with an average change in velocity of around 65 m/s, making the energy levels more suitable for the system.

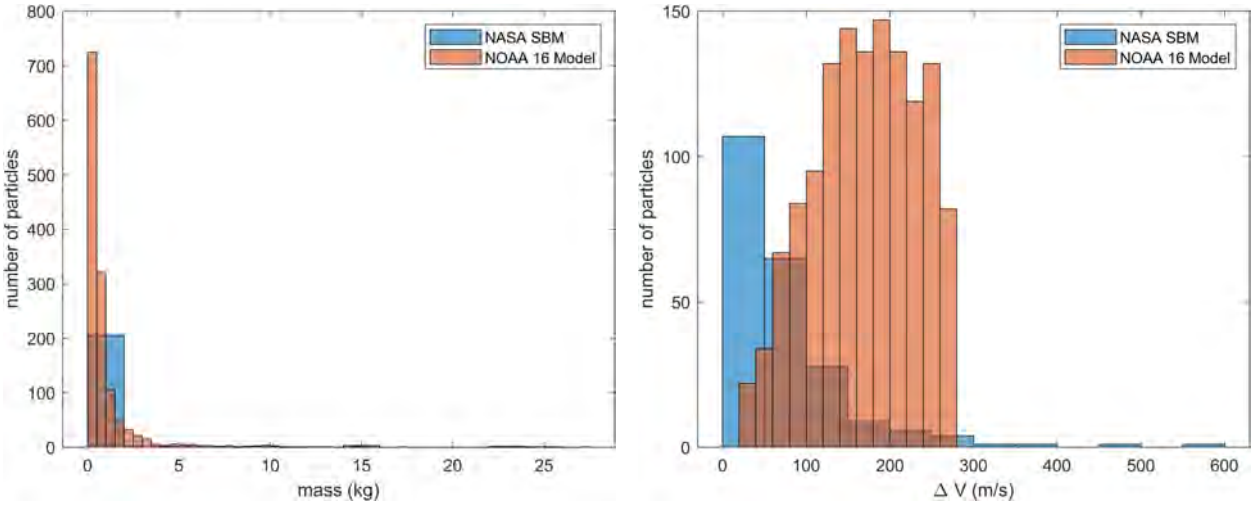

(a) Mass distributions of the fragments *(b)* Change in velocity distributions

Figure 2.11 Comparison of the Fragmentation Models computed

When analyzing the velocity distributions in terms of direction, the first method shows a spherical distribution shape (Figure 2.12a). Although the scalar values are widely distributed, most values are relatively high. Conversely, the NASA SBM distribution (Figure 2.12b) presents

more spikes distorting the distribution, but it better resembles a real explosion. Based on these observations, the explosions in this study are simulated by applying the NASA SBM.

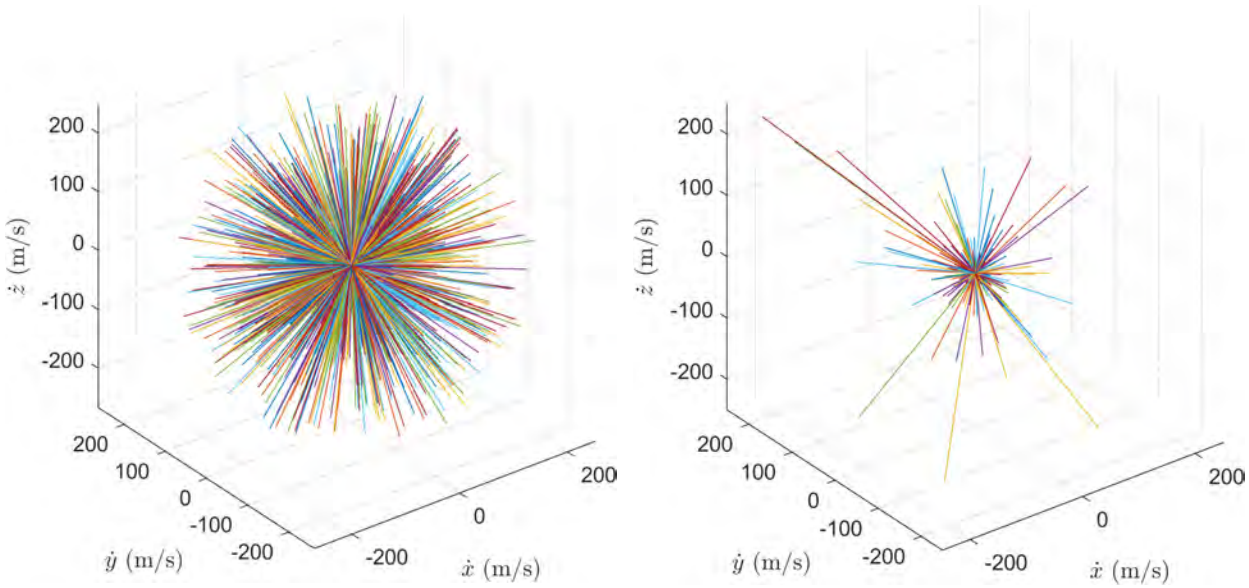

(a) NOAA 16 satellite battery explosion *(b)* NASA SBM

Figure 2.12 Explosion velocity distributions

3 Simulation

The simulation of the explosions requires some steps that are explained in this Chapter. Throughout the process, some databases are generated, saving memory and computation time when generating new case studies.

3.1 Fragmentation Event Set-Up

The computation of the explosions requires some initial conditions to be previously defined, such as the locations where the explosions are generated and the time of evolution to study the dispersion of the fragments.

- *Position of the break-up event*: Eight positions are defined as equally spaced in time throughout each orbit. The spacecraft is first located at the periapsis of the orbit, and the remaining locations are calculated by adding $1/8$ of the orbital period. This division not only segments the orbits into similar section, but also facilitates locating the spacecraft at specific positions, such as perilune or other significant regions of the orbit. Figure 3.1 illustrates the configuration of explosions for the study of L_1 and L_2 Lyapunov orbit families contained within the SoI of the Moon. The results of these simulations are presented in this research.

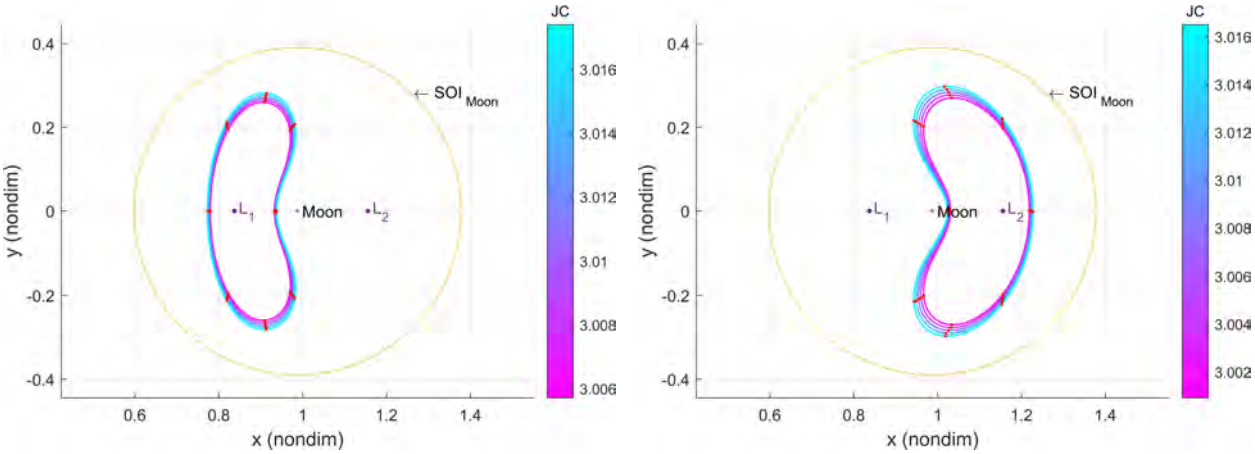

(a) Break-up positions in L_1 Lyapunov orbits *(b)* Break-up positions in L_2 Lyapunov orbits

Figure 3.1 Positions of the break-up events

- *Time of propagation*: Simulations are propagated over a time period of 2 years, with results plotted for both a short-term and long-term analysis. The short-term mode is established to include the first 50 days, encompassing the fragmentation events occurring approximately

in the first 20 days of propagation, and the subsequent debris evolution. The long-term mode extends to 2 years to analyze how debris continues to evolve over an extended period. This is set as the maximum time due to error propagation in the dynamical model for larger timescales.

These characteristics are fundamental to correctly set up the events, both for the pre and post-fragmentation.

3.2 Process to compute a fragmentation event

To assess the impacts of explosions, a few previous steps are necessary to compute fragmentation events. Such a process is presented in the flowcharts in Figures 3.2 and 3.3. The first step to proceed with the study is to generate an explosion. Some initial conditions related to the spacecraft and the orbits are required. Such initial conditions include the mass of the spacecraft m_{sat} and the state vector necessary to propagate the orbit using the $CR3BP$ ($\bar{s}$). The fragmentation event is also configured, defining three variables: the fragments' characteristic length to compute the *break-up model*, L_c, the time of evolution of the study, $t_{evolution}$, and the locations of the explosions, determined by equally dividing the period of the specific orbits, T/div, where *div* corresponds to the number of divisions (in this case, $div = 8$). The initial conditions of the orbits are defined by their state vector and period percentage, $[\bar{s}, t]$. The outputs of the break-up model, N_{tot} and $\overline{\Delta V}$, are used to propagate $\bar{s}$ during a specific time of evolution $t_{evolution}$. Each fragment is propagated using `ODE45`, obtaining an array of state vectors, $\bar{s}_{exp}$, containing the evolution of each particle for each time step, t_{exp}. Note that s_{exp} is a cell-array. The set of state vectors and time steps of each particle, *[$\bar{s}_{exp}$, t_{exp}]*, builds the explosion database.

A procedure is established to analyze the impact on the Cislunar region (Figure 3.3). Using the explosion database and selecting a specific time of evolution, the state vectors defined as $\bar{s}_{exp}$ included in $\bar{s}$ *debris* are classified based on whether the particles impact the Moon or Earth, escape the Earth-Moon system through Earth's SoI, or continue orbiting the region. The debris is classified computing `ODE` *events*, where all necessary parameters, such as the JC, mass, and ejection velocity of each fragment, are extracted for upcoming studies. These may be stored in a debris database.

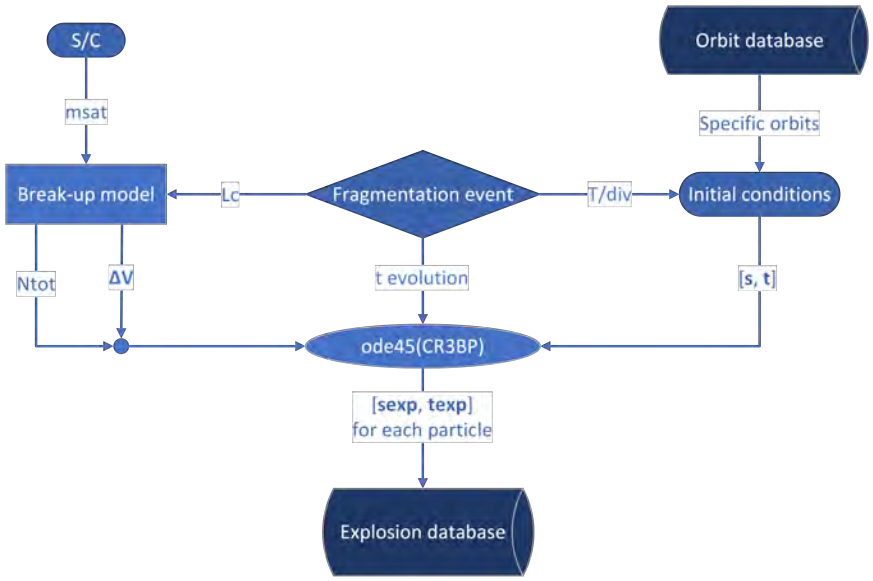

Figure 3.2 Procedure for the generation of the explosion

The effect on the Cislunar region is then assessed by examining the location of the debris, $\bar{s}_{exp}$, and studying their proximity to the Lagrange points, their evolution with respect to the Moon's SoI, and identifying patterns in their propagation. More studies are conducted on other orbits, analyzing the hazard zones and the probability of kill for other orbiting satellites. This involves examining both the likelihood of a fragment impacting a satellite and the probability of a satellite being destroyed by such an impact [12]. Understanding these effects helps to determine the safety of potential missions in the vicinity and may aid in the creation of policies for Cislunar traffic.

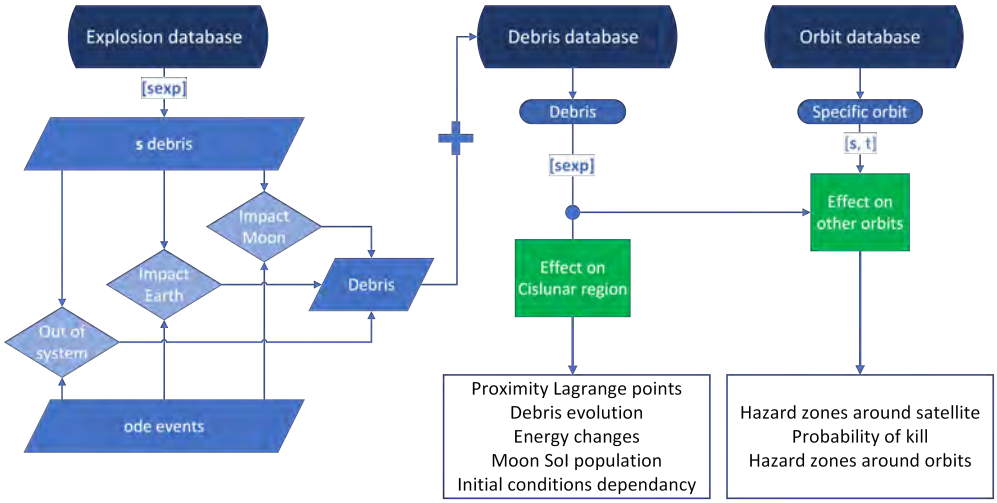

Figure 3.3 Procedure for the analysis of the impact on the Cislunar region

3.3 Generation of Databases

The local databases detailed above are created through the development of Graphical User Interfaces (GUIs) in `MATLAB`. There are three key databases in the process described in the next lines: the orbit database, the explosion database, and the debris database, as summarized in Figure 3.4.

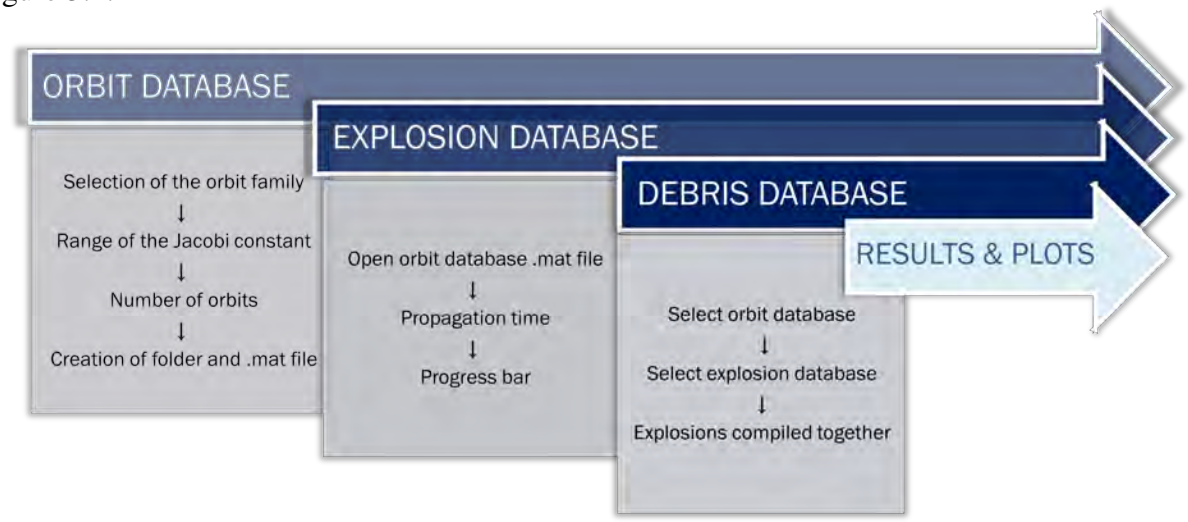

Figure 3.4 Generation of databases

First, for the orbit database, some initial conditions are required to be defined, to find the orbits that will be studied. The program creates a folder and saves a new file with the specific initial conditions, which are the state vectors where the fragmentation events will occur.

For the explosion database, the user is asked which files to open, so it is selected the one containing the desired orbit database. Next, the propagation time is selected. As an explosion usually takes a long time to compute, (it can be 20 minutes to 4 or more hours), a progress bar has been created so it is possible to predict how long it will take for the generation of the database to be completed.

After the different explosion data has been generated, and placed in separate files, it can then be recompiled as chosen by the user. It allows to conduct different analysis after the databases have been generated. For example, explosions from different family orbits could be studied at once, or some parameters could be analyzed, such as studying explosions at periapsis. Once explosions have been compiled together, plots are generated and results can be obtained.

3.3.1 Orbit Database

A pre-computed list of initial conditions (IC) includes some periodic orbit families. A new database is then created, called orbit database, which includes only the trajectories and IC that are relevant to the study. The orbit database starts through the selection of the orbits to be studied (Fig. 3.5). The program then generates a folder and saves a new file containing the specific IC that include the state vectors where the fragmentation events will occur in the selected orbits.

1. *Steps 1 and 2:* The user selects the initial conditions to propagate each orbit in a chosen family. This includes:
    - First, the family or families of orbits to be studied.
    - Secondly, a range for the Jacobi constant to identify specific orbits for the study.
2. *Step 3:* A list of the specific orbits selected is shown sorted in decreasing JC. The user then decides which orbits are included in the study.
3. *Step 4:* The program generates a folder and saves a .mat file containing the state vectors where the fragmentation events occur.

The orbit database is included in the .mat file called *ICD_Family_numberofexplosions.mat*, where *ICD* means "initial conditions data". Note that as the case of study computed in this research is set up for 8 explosions per orbit, depending on the number of orbits selected, a multiple of 8 is the total number of explosions. Figure 3.5 shows an example of 7 orbits, i.e., 56 explosions. If more than one family is selected for the study, this is also specified. For example, when selecting L_1 and L_2 Lyapunov orbits and DROs, *_L1L2DRO_* is the name specified in the *_Family_* of the .mat file.

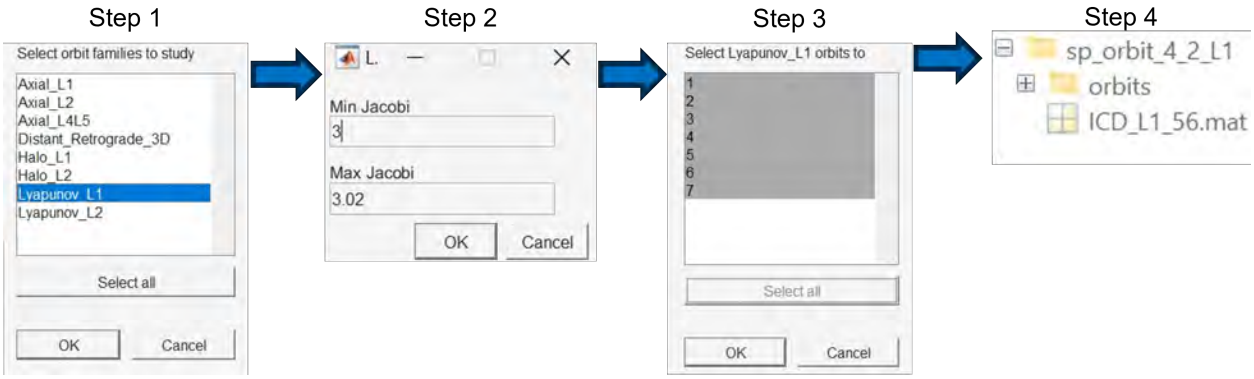

Figure 3.5 GUI for the computation of the orbit database

3.3.2 Explosion Database

To create the explosion database (Fig. 3.6), the user selects the desired orbit database file and specifies the propagation time. Since explosion computations take from 20 minutes to several hours, a progress bar is provided to estimate the completion time. Once the explosion data is generated and stored in separate files, it is recompiled based on user preferences, allowing for various analyses. For instance, explosions from different orbital families may be studied simultaneously, or specific parameters such as explosions at perilune. After compiling the explosion data, plots are generated, and results are obtained.

1. *Step 1:* The user selects the specific initial conditions obtained from the orbit database.
2. *Step 2:* The user specifies the propagation time. Suggested values are 50 days and 2 years for short- and long-term studies, but any time of interest in months may be entered.
3. *Step 3:* Explosions are calculated for each initial condition:
    - The increment of velocity and mass of each fragment is calculated using the NASA SBM.
    - Each particle is then propagated by applying the $CR3BP$.
4. *Step 4:* A separate file is created for each initial condition, storing the data of the initial conditions and fragments.

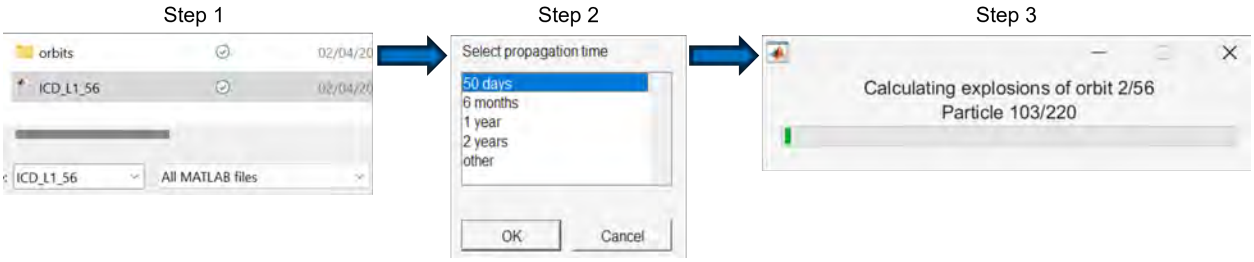

Figure 3.6 GUI during the computation of the explosion database

3.3.3 Debris Database

The debris database is used to classify and analyze the generated debris, focusing on their location, evolution, and proximity to key points like the Lagrange points and or collisions (Fig. 3.7).

This comprehensive database structure facilitates detailed analysis and enhances the understanding of debris behavior in the Cislunar region.

1. *Step 1:* The user selects one or more explosion databases.
2. *Step 2:* From the chosen explosion databases, the user may select all or specific explosions.
3. *Step 3:* The selected data is compiled for result analysis.
4. *Step 4:* Basic plots for understanding the system are generated and saved in a folder specified by the user. If the same folder is used in subsequent studies, comparison analyses will also be available.

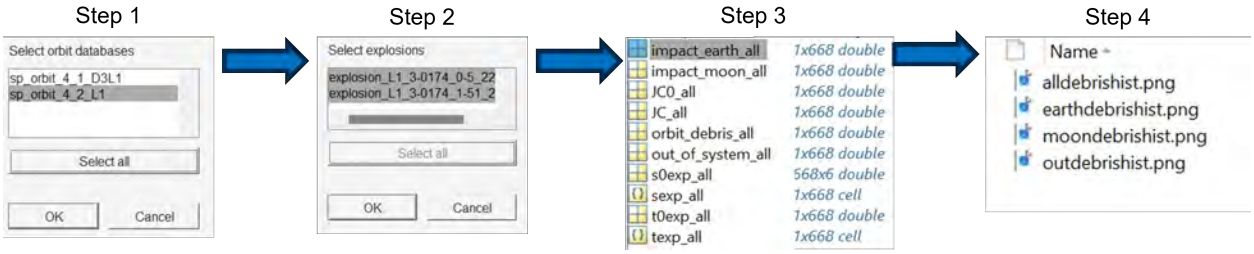

Figure 3.7 GUI to compute the debris database

4 Impact in the Cislunar region

The aforementioned methodology is applied for explosions in the orbit families L_1 and L_2 Lyapunov and DROs. The debris databases built are studied separately analyzing individual results for L_1 and L_2 Lyapunov orbits, and then comparing those results to conclude characteristics of debris behavior.

4.1 L_1 Lyapunov Orbits

In this case, 40 explosions are computed for 5 orbits of the family. Orbits are selected depending on the value of their Jacobi Constant, choosing the ones with close values to 3, as represented in Figure 3.1. This criterion is determined by looking into the size of the orbits and their close lunar passage.

4.1.1 Fragmentation Event

When the system starts to run, explosions occur as time goes by. The fragmentation events take place during approximately one period of the orbits, i.e., around 17 days, presented in Figure 4.1.

In the first plot of Figure 4.1a, the first explosions have just occurred, so particles are not dispersed yet. Although a change in velocity has been applied to the particles, it is observed that at the beginning, they follow a similar path to the original orbits in a clockwise direction. When they arrive at the periapsis zone, particles start to disperse, and so on as time advances.

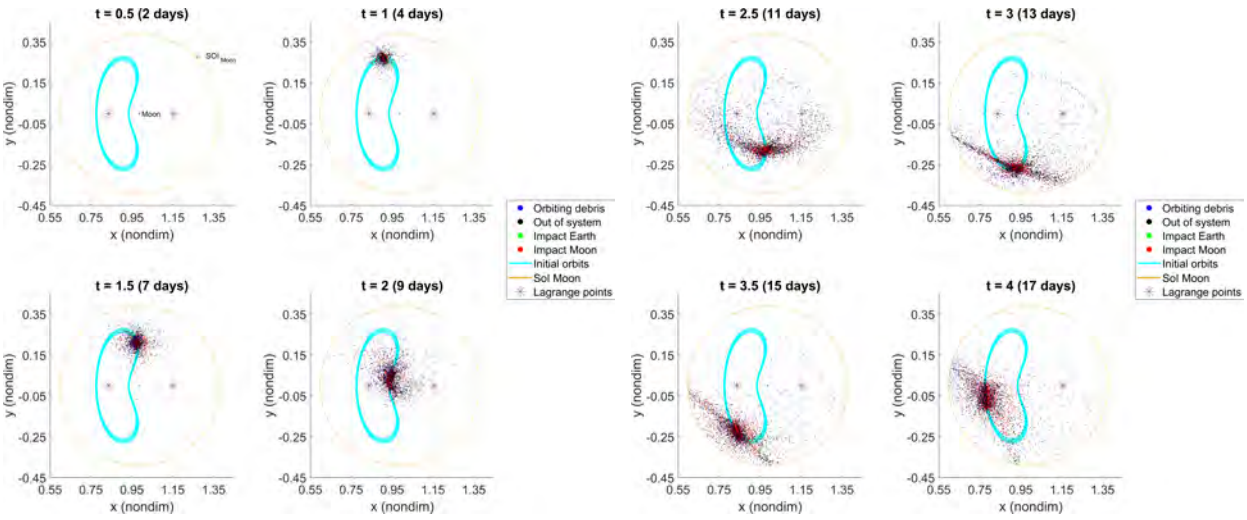

(a) First 20 explosions propagated *(b)* All explosions propagated

Figure 4.1 Debris evolution during 40 fragmentation events along 5 L_1 Lyapunov orbits

Figures 4.1a and 4.1b only represent the debris inside the Sphere of Influence of the Moon and in the last plots, it is observed that the fragments that remain inside are mostly the ones that will impact the Moon at some point in the study.

4.1.2 SoI Moon

Figure 4.2 represents the evolution of debris inside the Sphere of Influence of the Moon throughout all the time of propagation. Figure 4.2a represents the short term with plots for 5, 10, 30, and 50 days. The long term appears in Figure 4.2b, represented by plots for 3 months, 6 months, 1 year, and 2 years.

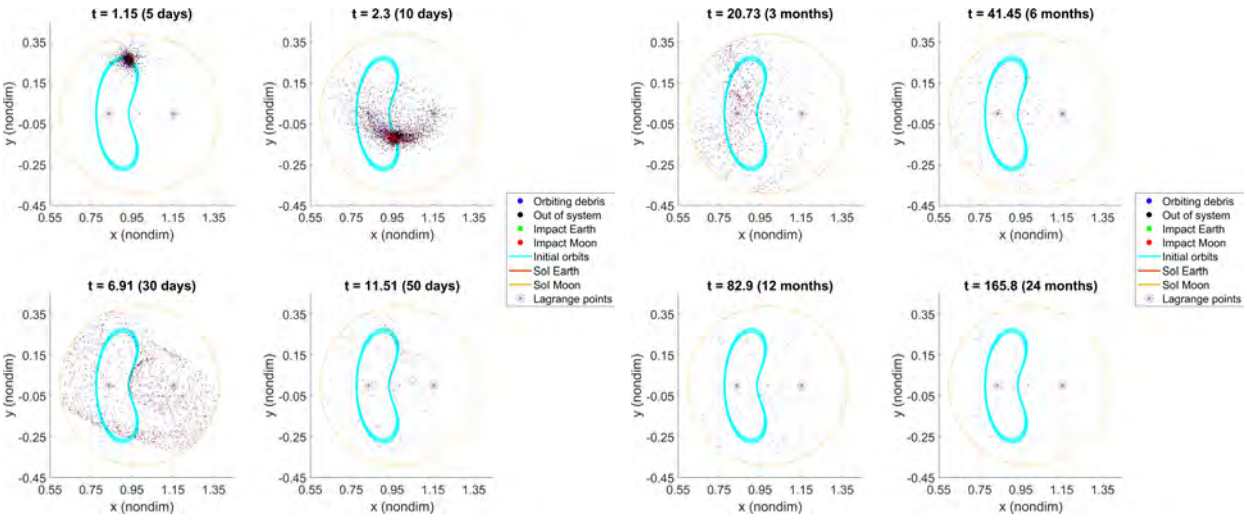

(a) Short term *(b)* Long term

Figure 4.2 Debris evolution over 2 years inside the Moon's SoI for L_1 Lyapunov explosions

During the first 30 days, there is still a lot of debris in the region of study, but as time goes by, the amount of debris decreases drastically, and at the end of the study, almost all the debris that is supposed to impact the Moon or go out of the system, has already done it.

4.1.3 Debris Evolution

Figures 4.3a and 4.3b represent the debris propagation for the short and long term, respectively. The color of the debris depends on its type:

- *Green fragments*: debris impacted by the Earth;
- *Red fragments*: debris impacted by the Moon;
- *Black fragments*: debris escaping the system, i.e., the Sphere of Influence of the Earth;

- *Blue fragments*: debris orbiting through the region.

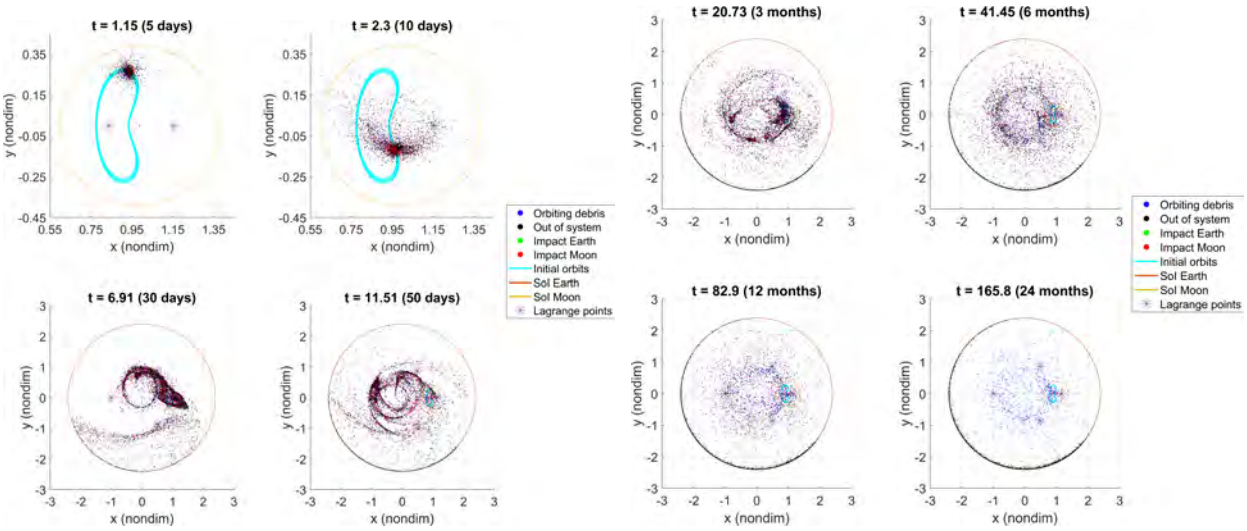

(a) Short term simulation *(b)* Long term simulation

Figure 4.3 Debris simulation over 2 years for explosions in L_1 Lyapunov orbits

Although explosions occur in lunar orbits, the change in the velocity applied to each fragment pushes most of them out of the system, while the rest mostly enter orbits around the Earth, which is the main body of the system. This is observed after 30 days of evolution in Figure 4.3a.

When analyzing the long term evolution, it is observed in Figure 4.3b that after two years, the amount of debris in the Cislunar region has decreased drastically compared to the first months after the fragmentation events.

4.1.4 Type of debris

It is observed in Figure 4.4 that many fragments impact the Moon straight after the explosions, and the rest mostly remain inside the system. The amount of debris that escapes the system evolves at a more constant pace. A small and neglectful amount of them end up impacting the Earth.

It was thought that mass could be one of the main parameters affecting the behavior of debris. Figure 4.5 shows the distribution of masses for the different final states the debris is classified in. It is observed that the percentages are closely similar for each column, just varying in the fragments impacted by the Earth. However, the sample of debris that impacts the Earth, less than 10 is not enough to obtain any conclusion.

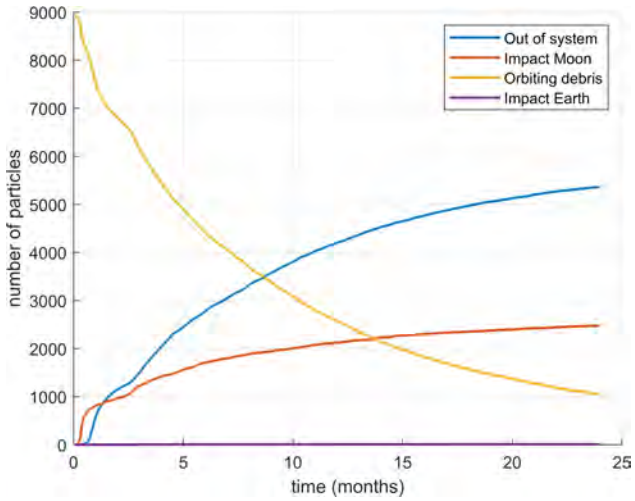

Figure 4.4 Evolution of debris through the time of study for L_1 Lyapunov explosions

According to the plot in Figure 4.5, no patterns are found, concluding that differences in mass have a small, if any, impact on the outcome of where debris is directed.

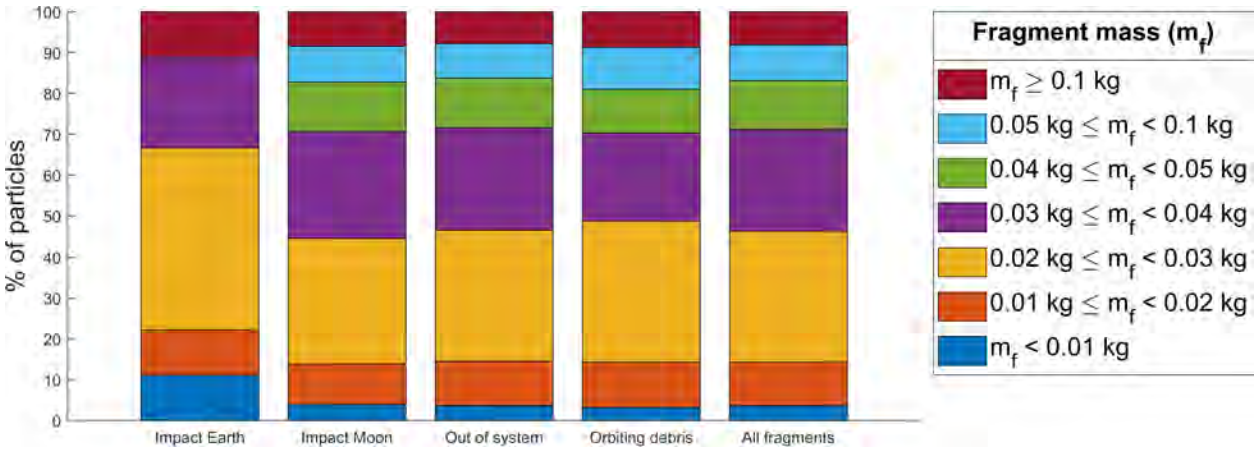

Figure 4.5 Debris evolution in terms of mass after 2 years for L_1 Lyapunov explosions

4.1.5 Debris trajectories

The plots presented in Figures 4.7 and 4.8 illustrate the trajectories of particles over the short term, defined as 50 days. The particles have been divided into five groups based on their energy levels and JC. This classification adheres to the explanation in Section 2.1.4. Specifically, depending on the JC, fragments are confined to specific regions within the Cislunar region, revealing certain patterns.

The change in the Jacobi constant is represented for each fragment in Figure 4.6 compared to the JC of the initial orbits. For most of the debris, there is a slight variation in the JC, while for the ones that impact the Earth, the change is much bigger. The fragments' JC tends to decrease rather than increase. The distribution of the JC is evident in the trajectories related to the $ZVCs$. As the JC decreases, more trajectories are plotted, and their behavior becomes increasingly chaotic.

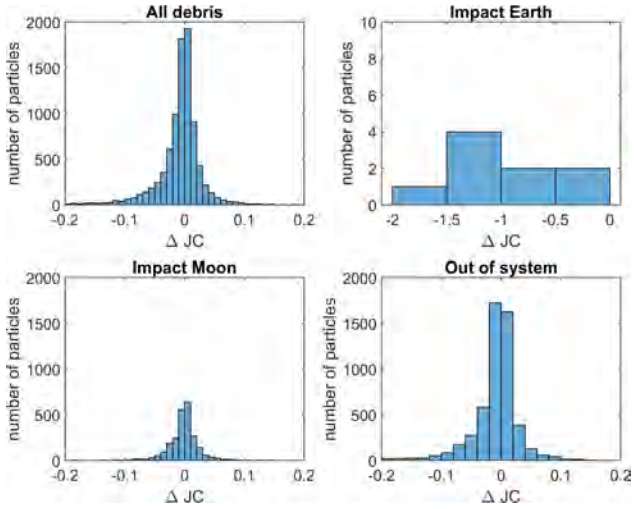

Figure 4.6 Change in the JC of each fragment created in L_1 Lyapunov explosions

A higher JC means lower orbital energy, resulting in more restricted motion constrained by $ZVCs$ [19]. Each plot in Figure 4.7 displays two $ZVCs$, one for fragments with the highest JC, i.e., the most restrictive. The other one is for those with the lowest JC, which is included for reference, as most fragments can cross it. Fragments with higher JC are presented in Figure 4.7a, follow very restrictive $ZVCs$ and most of them exhibit lower velocities. The combination of these factors results in the majority of these fragments colliding with the Moon. In the cases presented in Figures 4.7b, 4.7c and 4.7d, the velocities are higher, leading to greater dispersion of the fragments.

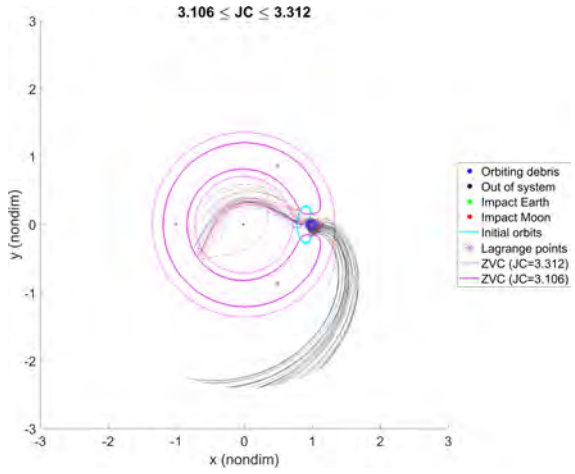

(a) $ZVCs$ for JCs of 3.312 and 3.106

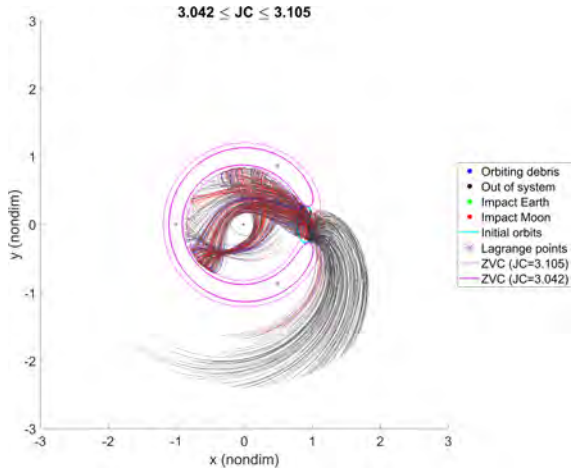

(b) $ZVCs$ for JCs of 3.105 and 3.042

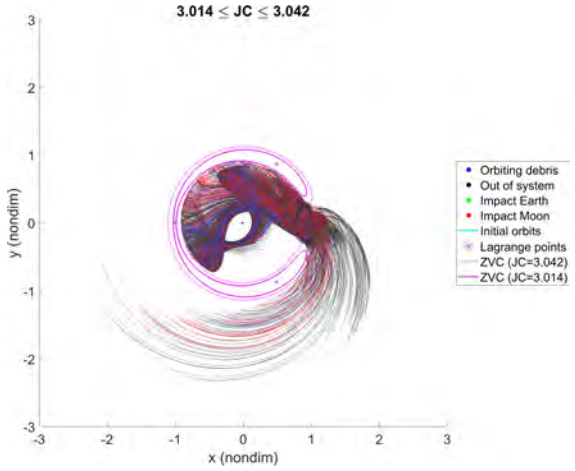

(c) $ZVCs$ for JCs of 3.042 and 3.014

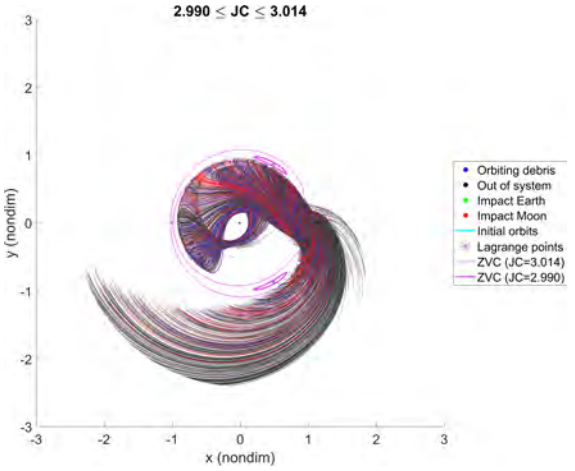

(d) $ZVCs$ for JCs of 3.014 and 2.990

Figure 4.7 Short term fragment trajectories bounded by $ZVCs$ (L_1 Lyapunov explosions)

However, due to the presence of the Earth and the narrow escape routes within the forbidden regions defined by the $ZVCs$, there is a noticeable division into two groups of particles: those outside the ZVC, most of which will escape the system, and those that remain inside, orbiting the Earth. Over two years, some of the latter fragments also manage to find a path to go out.

The scenario presented in Figure 4.8 involves fragments with the highest orbital energy levels, which are not restricted by any ZVC. Their behavior is more chaotic and dispersed throughout the Cislunar region. Nonetheless, a division is still apparent, as some particles adopt more distant, circular orbits and escape the system, while others are attracted to Earth, resulting in more erratic behavior.

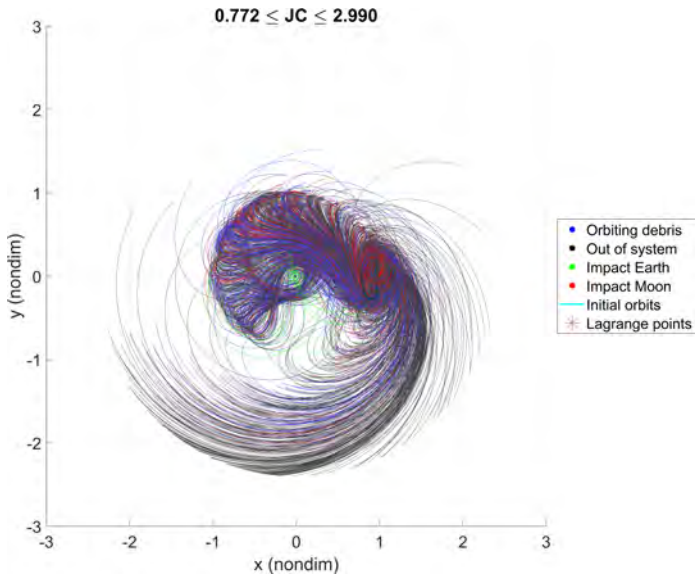

Figure 4.8 Short term fragment trajectories without constraints (L_1 Lyapunov explosions)

4.1.6 Return maps

This section illustrates the first and second passages of fragments through various planes of interest. This provides different perspectives to confirm the conclusions drawn from the standard plane of this study where $z = 0$. A consistent pattern is observed across all planes regarding the three-dimensionality of particle trajectories. The initial orbits are planar, but explosions push the fragments along the $\hat{z}$-axis. However, as fragments are propagated across planes, their return trajectories tend to decrease the $\hat{z}$-axis coordinate, leading to the particles regrouping around the plane of the initial orbits, i.e., the XY plane.

Figure 4.9a illustrates a plane perpendicular to the $\hat{x}$-axis containing the Earth. In the first pass, two groups of particles are noticeable. The first group consists of the fragments within the region bounded by the $ZVCs$, with $\hat{y}$ values ranging from -1 to 1. Upon return, these fragments exhibit a symmetric distribution centered on Earth but in equal quantities. The second group is positioned between $\hat{y}$ values of -2 and -1, outside this region. Many of these particles already escape the system before returning to this plane.

A different plane perpendicular to the $\hat{x}$-axis is depicted in Figure 4.9b. However, in this instance, it contains the Moon. Fragments pass very near the Moon during the first passage, but upon return, particles have either been attracted to it or are situated in much more distant orbits.

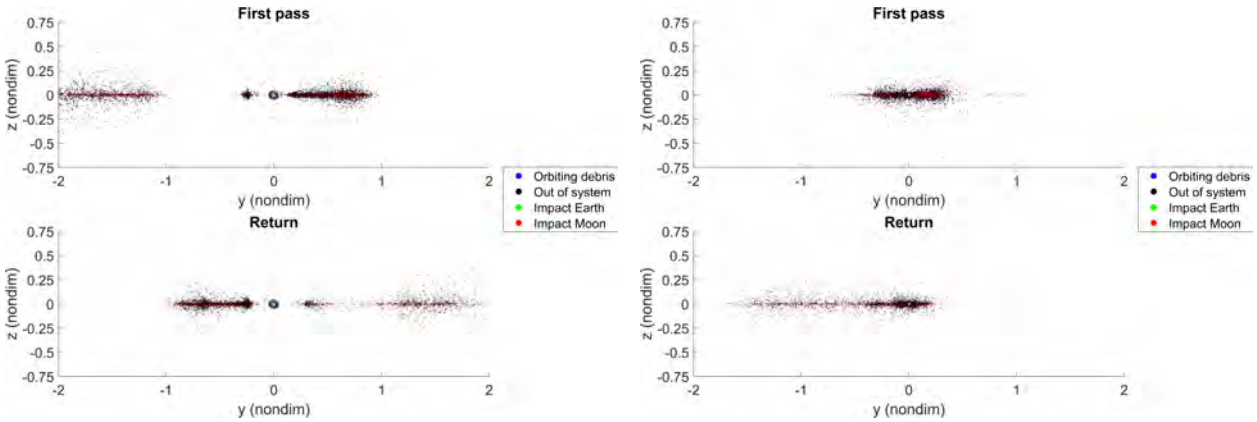

(a) Plane containing the Earth *(b)* Plane containing the Moon

Figure 4.9 Return map in the $x = 0$ plane (L_1 Lyapunov explosions)

The last scenario, presented in Figure 4.10, involves a plane perpendicular to the $\hat{y}$-axis containing the Earth, the Moon, and L_1, L_2 and L_3 Lagrange points. The region near the Moon is the most chaotic, due to the influence of the Moon's gravitational force and the occurrence of explosions. Furthermore, in the vicinity of the Moon is where the $ZVCs$ open up, facilitating the exchange of fragments between the interior and exterior regions of these curves.

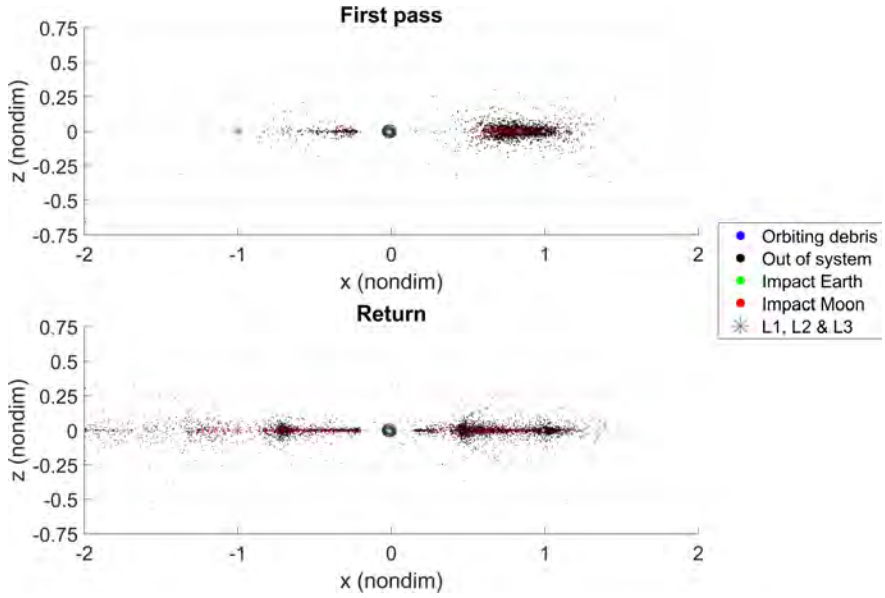

Figure 4.10 Return map in the $y = 0$ plane (L_1 Lyapunov explosions)

4.1.7 Density maps

The density maps presented in Figures 4.11 and 4.12 depict the regions within the Cislunar region that experience the highest debris traffic over the entire propagation period, which spans two years from the start of the simulation. The XY plane is divided into square surfaces with dimensions of $3,844 \times 3,844$ km. The position of each of the $8,905$ fragments is recorded at defined timesteps, separated by 0.01 in dimensionless time, corresponding to approximately one hour.

The accumulation of particles at the explosion points, coupled with the limited initial dispersion observed in Section 4.1.1, results in the initial orbit being clearly defined and containing the highest number of fragments as plotted in Figure 4.11. Another path with the highest particle accumulation is a ring around the Moon. As shown in Figure 4.4, about $1/3$ of the fragments impact the Moon. The ring is also illustrated in Figure 4.7a, which means that the lower-orbital energy particles form the ring. Most of the particles present a JC around 3, and it is observed that the space region restricted by the $ZVCs$ for this JC is characterized by sparse accumulation. This region bounds the particles confined within the area of Earth's greater influence. Debris follows paths that move from one boundary to another without approaching the Earth excessively. The closest area to Earth is the region with the fewest debris flows in the entire space.

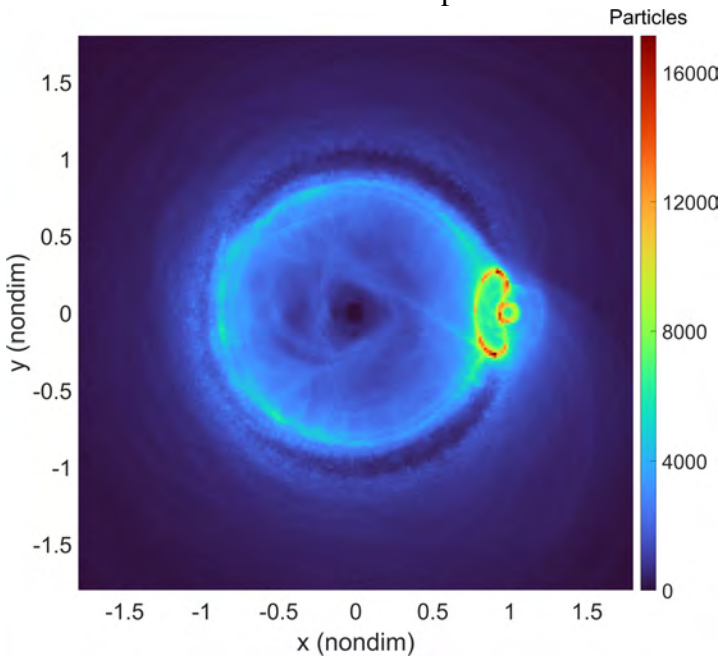

Figure 4.11 Density map of debris evolution over 2 years (L_1 Lyapunov explosions)

Figure 4.12 plots the same graph but divides the particles according to the coordinates in the orbit where the explosion occurs. Generally, it is observed that after the explosion, the particles remain accumulated along the orbital path for approximately a quarter of the orbit before dispersing, creating very similar patterns. The main difference is observed in the bottom right plot of Figure 4.12a. It shows the fragments created by explosions at the periapsis of the orbits. In this case, the Moon exerts a significant influence due to its proximity, causing most of the particles to collide with it. From this observation, it is inferred that the least problematic scenario regarding the safety of the region is that the explosion occurs near the periapsis of the Lyapunov orbit as most of the resulting fragments quickly collide with the Moon, leaving less debris in orbit.

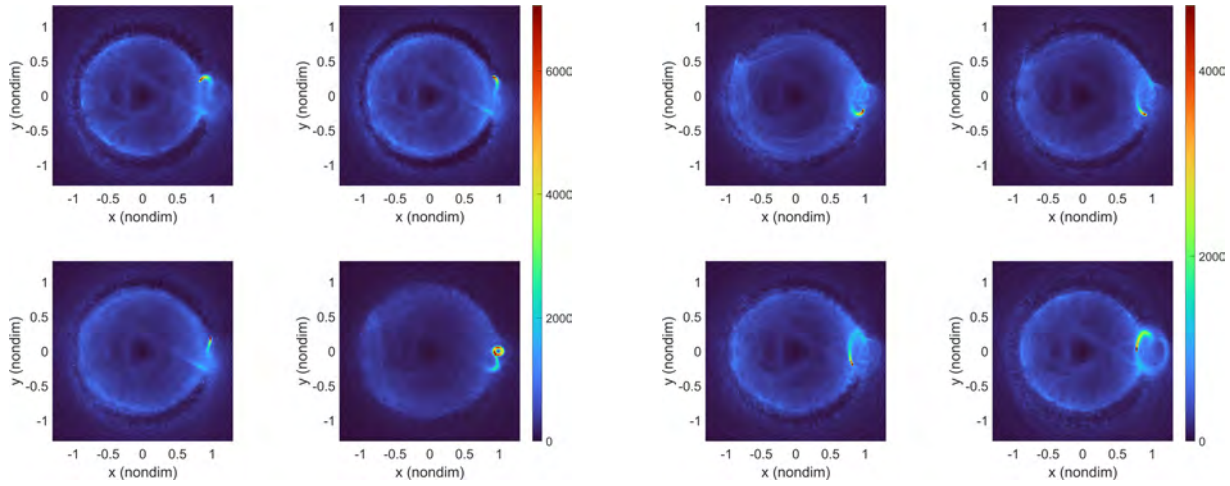

(a) First four ICs *(b)* Rest of ICs

Figure 4.12 Density maps for different ICs (L_1 Lyapunov explosions)

4.2 L_2 Lyapunov Orbits

The same simulation computed before is repeated for explosions occurring in L_2 Lyapunov orbits following the criteria explained for the L_1 Lyapunov simulation. The fragmentation event for this case is also presented in Figure 3.1.

4.2.1 Fragmentation Event

The fragmentation events take place during approximately one period of the orbits, i.e., around 17 days, the same as in the previous case. Assuming the Moon as a center of symmetry, the propagation presented in 4.13 is symmetrical to the one observed for the L_1 Lyapunov explosions.

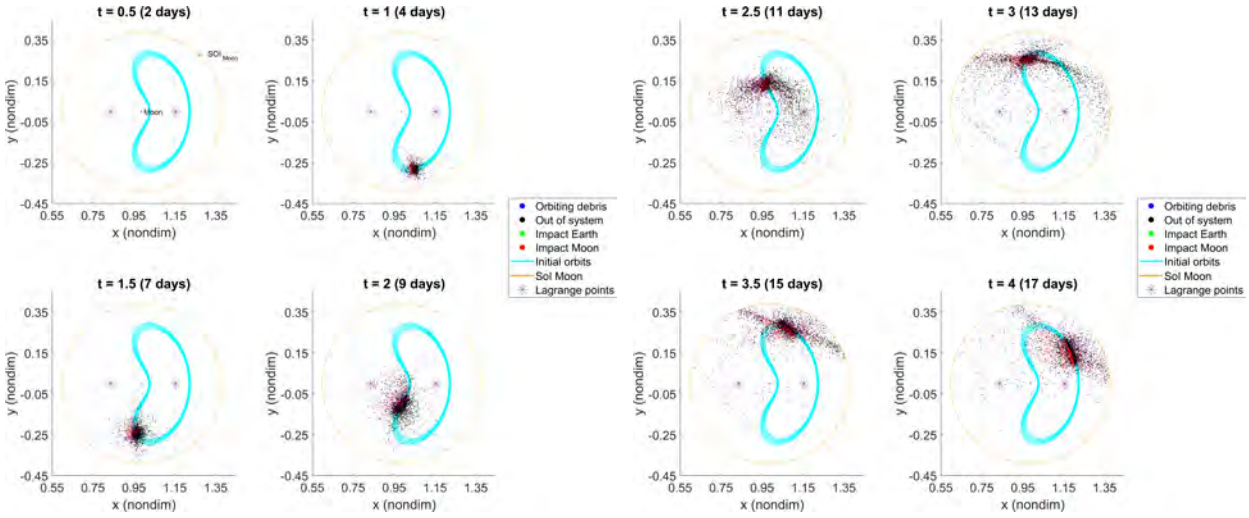

(a) First 20 explosions propagated *(b)* All explosions propagated

Figure 4.13 Debris evolution during 40 fragmentation events along 5 L_2 Lyapunov orbits

4.2.2 SoI Moon

Figure 4.14 represents the evolution of debris inside the Sphere of Influence of the Moon throughout all the time of propagation. From day 30, it is seen that the system is no longer symmetrical. Right after the explosion, the Moon is the main body of the problem, so particles behave similarly. However, as time goes by, the Earth's attraction has a deeper role in the system dynamics. Fragments leave the Moon SoI from different positions and directions. It causes that in this case, much fewer particles remain in the Moon SoI after the first stages.

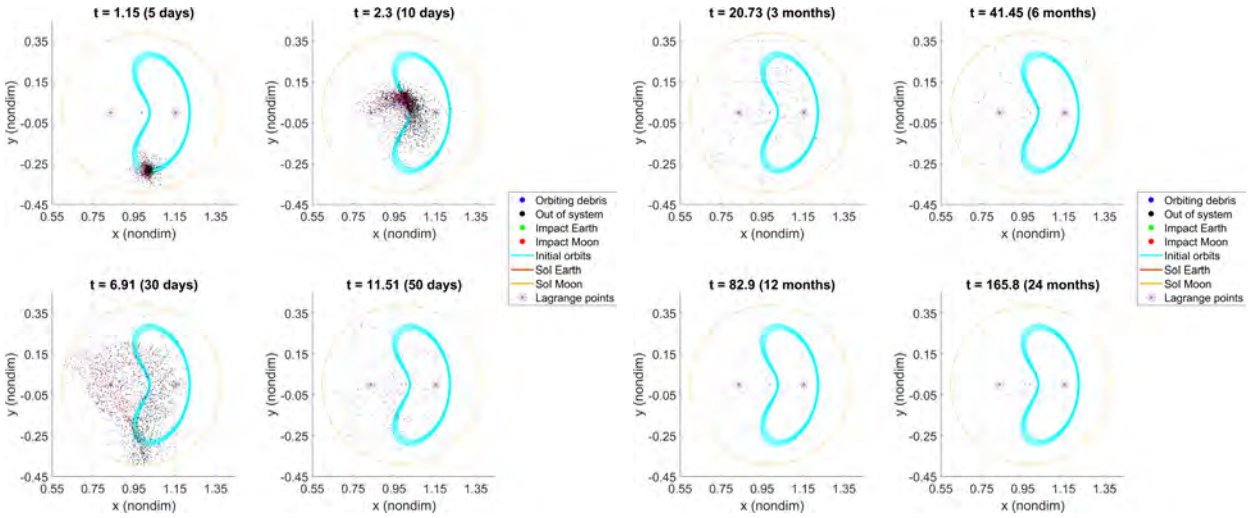

(a) Short Term *(b)* Long Term

Figure 4.14 Debris evolution over 2 years inside the Moon's SoI for L_2 Lyapunov explosions

4.2.3 Debris Evolution

Figures 4.15a and 4.15b represent the debris propagation for the short and long term, respectively. Looking into short term evolution in 4.15a, debris is expelled from Moon SoI more rapidly, with an early massive amount of particles in an escape trajectory already by day 30^{th}. In long term evolution, it is observed that particles that remain in the system engage in orbits that are further apart from the Earth than in the previous case.

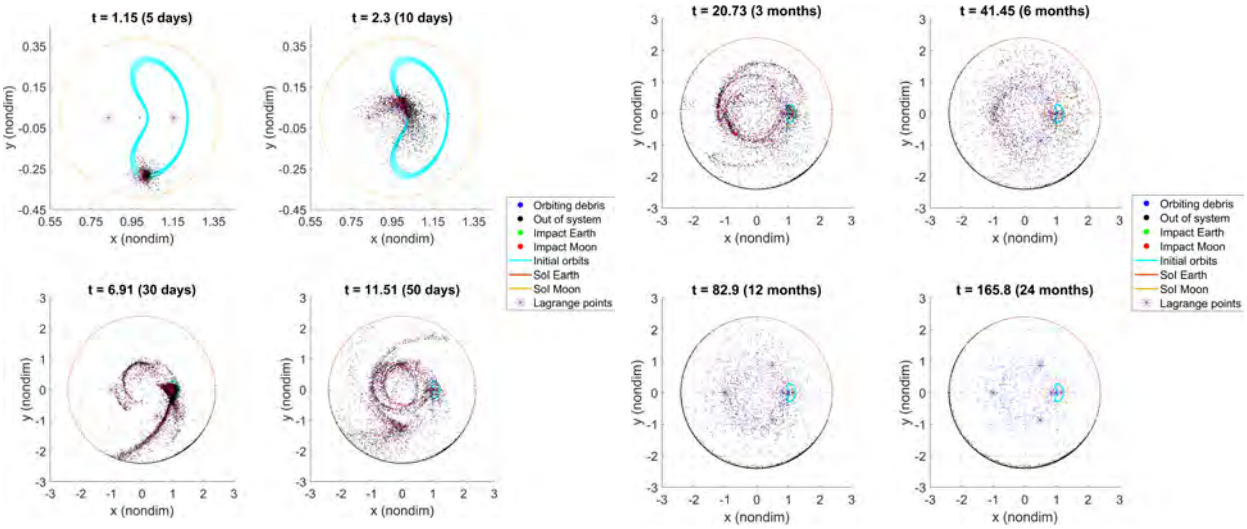

(a) Short term simulation

(b) Long term simulation

Figure 4.15 Debris simulation over 2 years for explosions in L_2 Lyapunov orbits

4.2.4 Type of debris

Analysing Figure 4.16, it is observed that right after the fragmentation events occurred, a large number of fragments had already escaped the system. This is explained due to the initial orbits being in the vicinity of L_2, which is closer to the boundary of the system.

According to the plot in Figure 4.17, no patterns are found, leading to the same analysis that was made in the previous case of study. No influence on the mass of each fragment has been found in the outcome of the simulation.

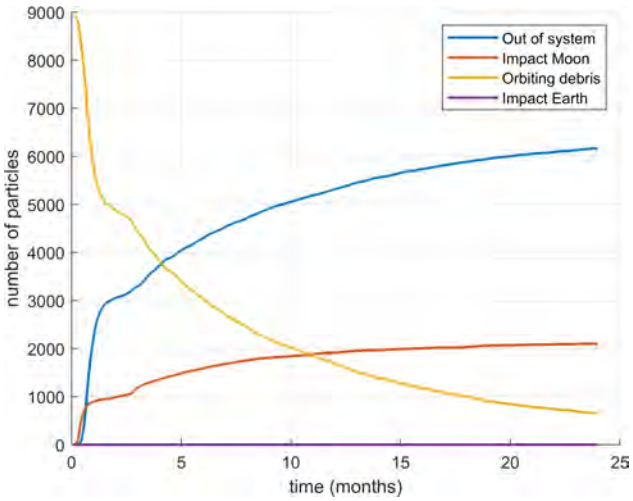

Figure 4.16 Evolution of debris through the time of study for L_2 Lyapunov explosions

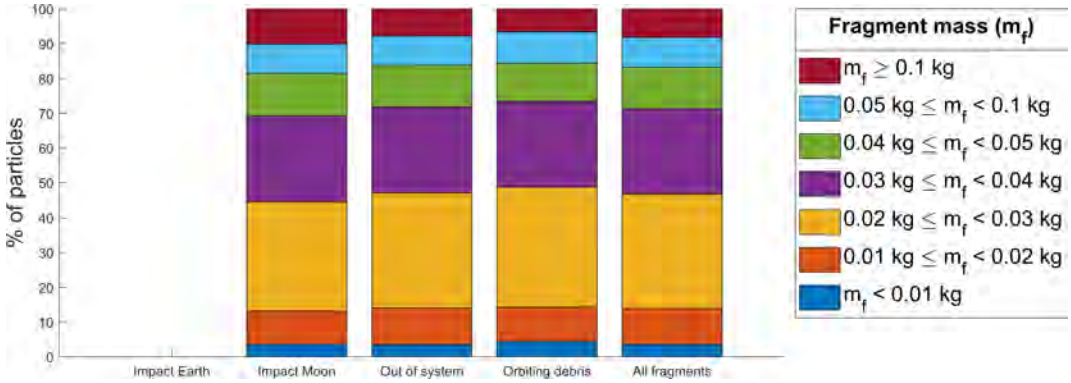

Figure 4.17 Debris evolution in terms of mass after 2 years for L_2 Lyapunov explosions

4.2.5 Debris trajectories

Similar to the L_1 Lyapunov case, trajectories are illustrated in Figures 4.18 and 4.19. Fragments with more restrictive $ZVCs$ in Figure 4.18a impact the Moon. This effect is even more pronounced due to the greater number of particles with a high value of their JC. In the remaining plots, similar behavior is observed in the way the debris evolves, although it is already evident that fewer fragments remain in the region near the Earth. This is explained because the L_2 Lyapunov orbits are close to the L_1 Lyapunov orbits but facing the opposite direction, on the side of the Moon farthest from the Earth. Starting from that side of the system, the $ZVCs$ create a sort of funnel that makes it more difficult for debris to enter that zone of the Cislunar region.

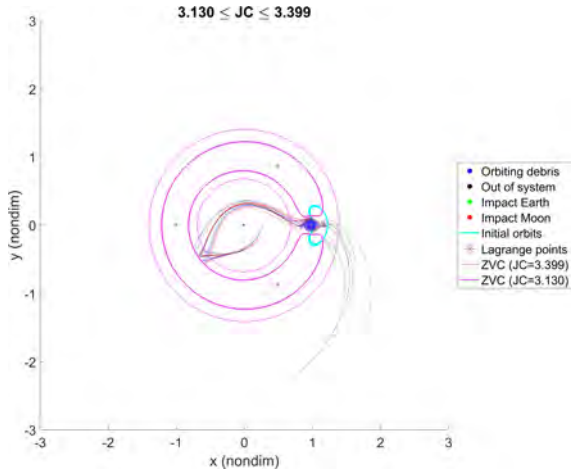

(a) $ZVCs$ for JCs of 3.399 and 3.130

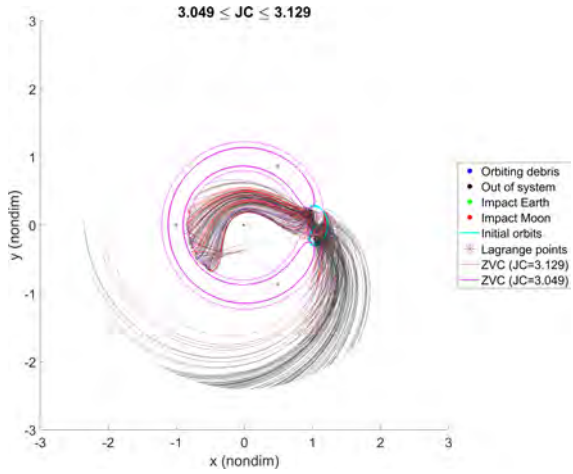

(b) $ZVCs$ for JCs of 3.129 and 3.049

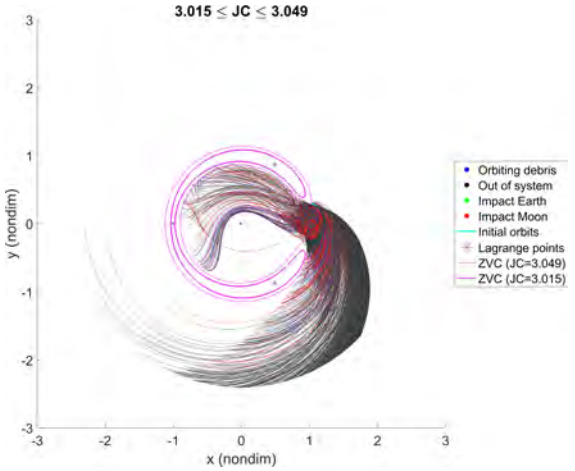

(c) $ZVCs$ for JCs of 3.049 and 3.015

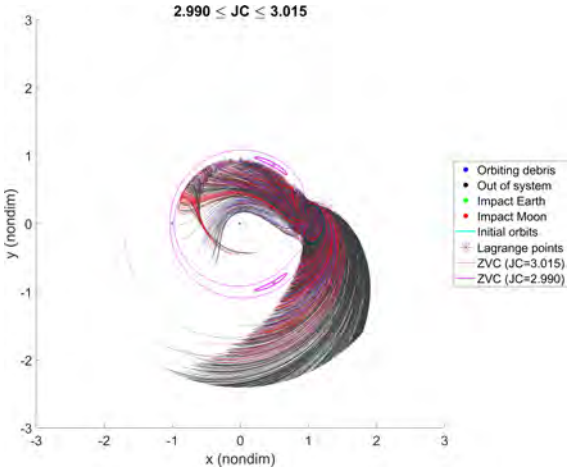

(d) $ZVCs$ for JCs of 3.015 and 2.990

Figure 4.18 Short term fragment trajectories bounded by $ZVCs$ (L_2 Lyapunov explosions)

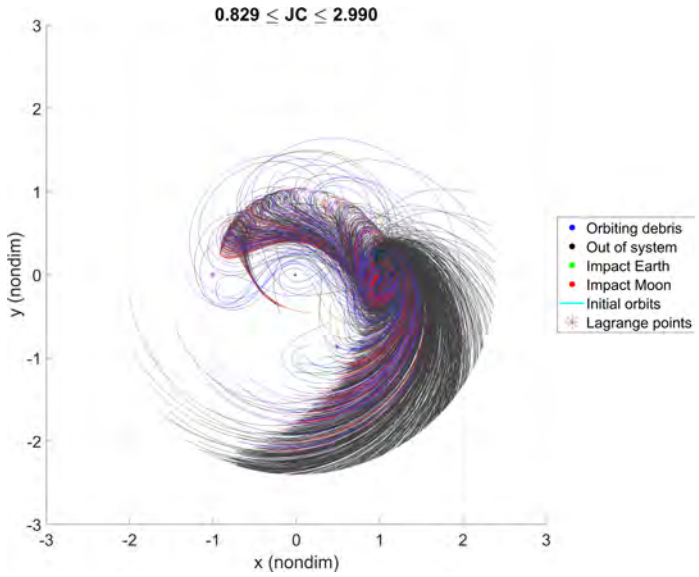

Figure 4.19 Short term fragment trajectories without constraints (L_2 Lyapunov explosions)

The change in the Jacobi constant is represented for each fragment in Figure 4.20. As shown for the L_1 Lyapunov study case, the fragments' JC tend to decrease rather than increase and as the JC decreases, more trajectories are plotted, resulting in more chaotic trajectories.

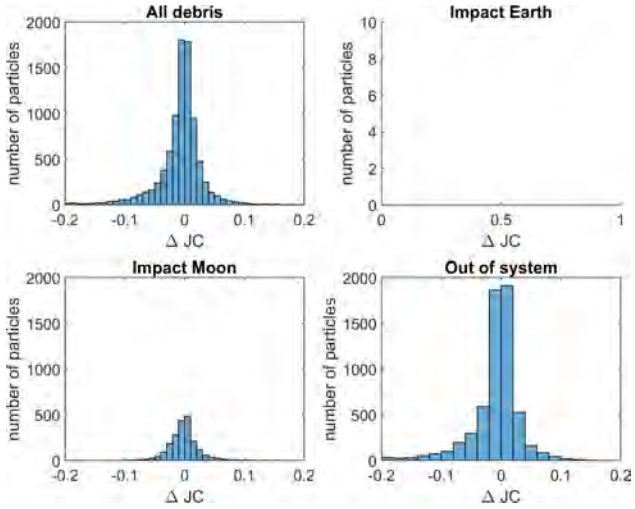

Figure 4.20 Change in the Jacobi Constant of each fragment in L_2 Lyapunov explosions

4.2.6 Return Maps

The same maps previously presented for the ICs of L_1 Lyapunov are presented again, focusing on the same planes of interest. Figure 4.21 shows that the behaviors observed in Section 4.1.6 are extrapolated to this case. Note that the number of particles farther from the observed celestial bodies, both the Earth and the Moon, has increased significantly. Due to the difference in initial positions and trajectories, the fragments are more restricted in accessing the area inside the $ZVCs$.

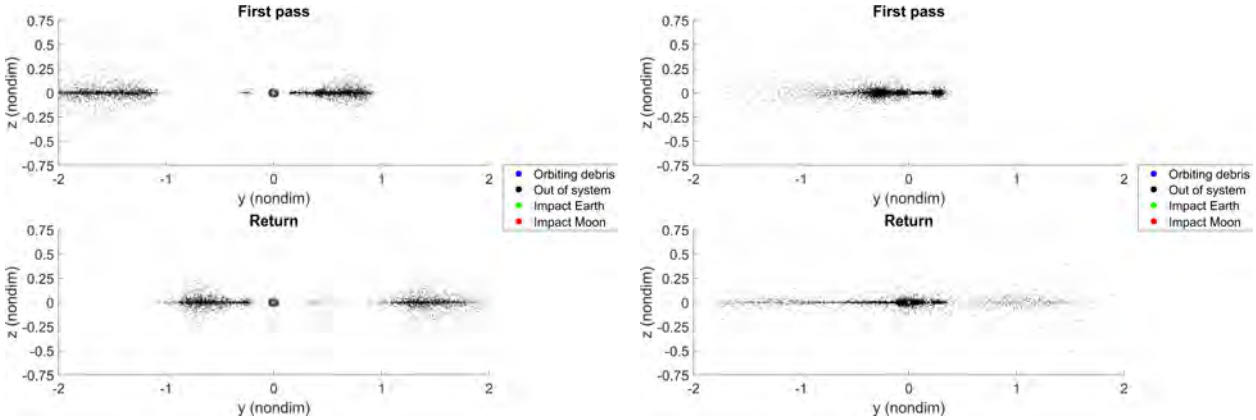

(a) Plane containing the Earth *(b)* Plane containing the Moon

Figure 4.21 Return map in the $x = 0$ plane (L_2 Lyapunov explosions)

In the case of the plane where $y = 0$, Figure 4.22 shows a significant group of particles crossing

this plane for the first time with a negative $\hat{x}$ coordinate. As previously mentioned, this is due to the restrictions imposed by the $ZVCs$, keeping the particles in the region between the Earth and the Moon.

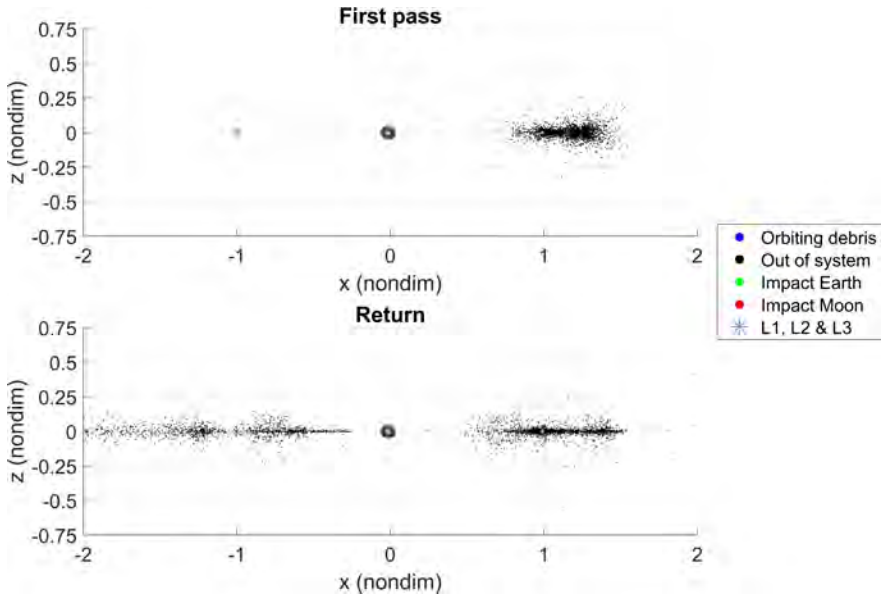

Figure 4.22 Return map in the $y = 0$ plane (L_2 Lyapunov explosions)

4.2.7 Density maps

The density maps applied to the explosions occurring in L_2 Lyapunov orbits are presented again. The parameters and considerations introduced in Section 4.1.7 are maintained.

Figure 4.23 reveals that the highest concentration of fragments occurs along the path of the initial orbit and in a ring around the Moon, where the particles eventually impact. The presence of the $ZVCs$ is noticeable, as the region of space restricted by these curves is less populated. The colors representing a low accumulation of fragments predominate in this plot. This is because, after 50 days, 41.32% of the fragments are no longer orbiting in the region of study, with most of them expelled from the system. Consequently, a high presence of debris is not observed.

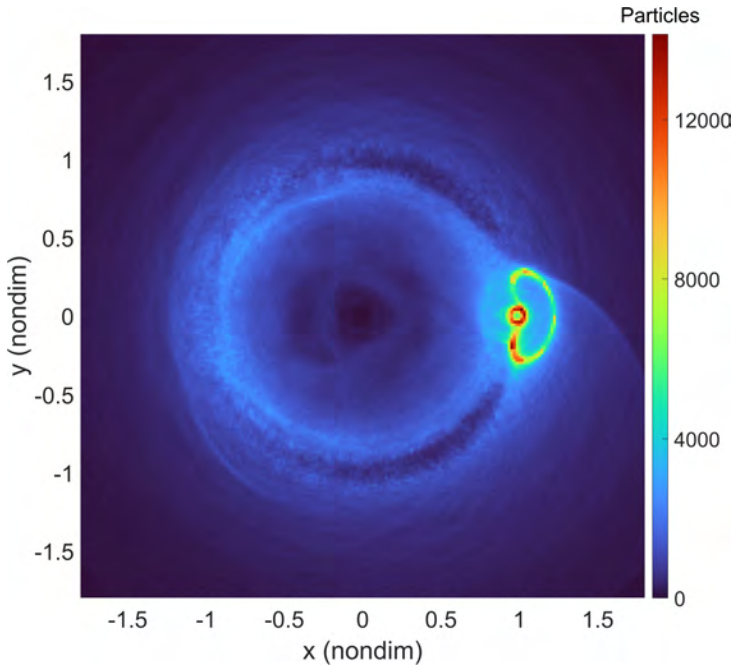

Figure 4.23 Density map of debris evolution over 2 years (L_2 Lyapunov explosions)

The debris generated from explosions near the periapsis of the orbit illustrated in the lower left plot of Figure 4.24a, quickly collide with the Moon, reducing the impact observed in the Cislunar region. Additionally, it is observed that explosions occurring at positions before the periapsis, represented in Figure 4.24b, result in a small accumulation of debris in the observed region. The fragments generated in these positions are forced out of the system. Due to the trajectory that fragments acquire from the ejection velocities, debris is pushed into areas restricted by their energy levels, preventing them from accessing the area between the Moon and the Earth.

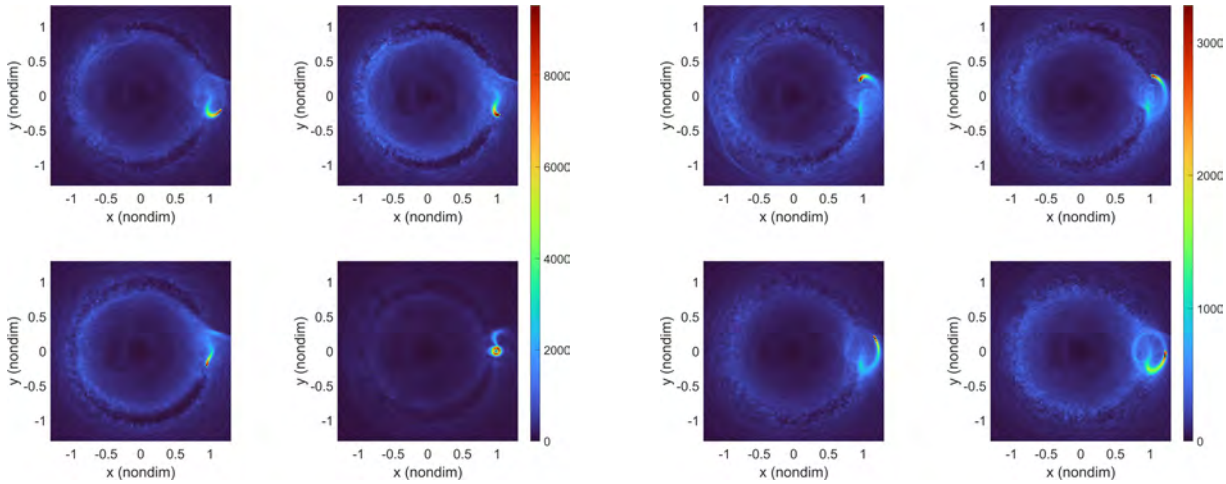

(a) First four ICs *(b)* Rest of ICs

Figure 4.24 Density maps for different ICs (L_2 Lyapunov explosions)

4.3 Comparison between orbit families

In order to better analyze the results of both cases, other plots are obtained to make the comparison more visual.

Figure 4.25 shows a comparison of how the debris evolves, both in the short and long term for the fragmentation events previously computed. As mentioned above, the main difference is that, in the case of L_2 Lyapunov orbits, the number of fragments escaping from the system is much higher than in the case of L_1 Lyapunov orbits. However, when looking at the long term, results are very similar for both cases. How the fragments interact with the gravity of the Earth and the Moon is very similar in the long term for both orbit families. Thus, it is concluded that the large number of particles that escape at the beginning of the explosions of the L_2 Lyapunov is mainly due to its proximity to the boundary of the system.

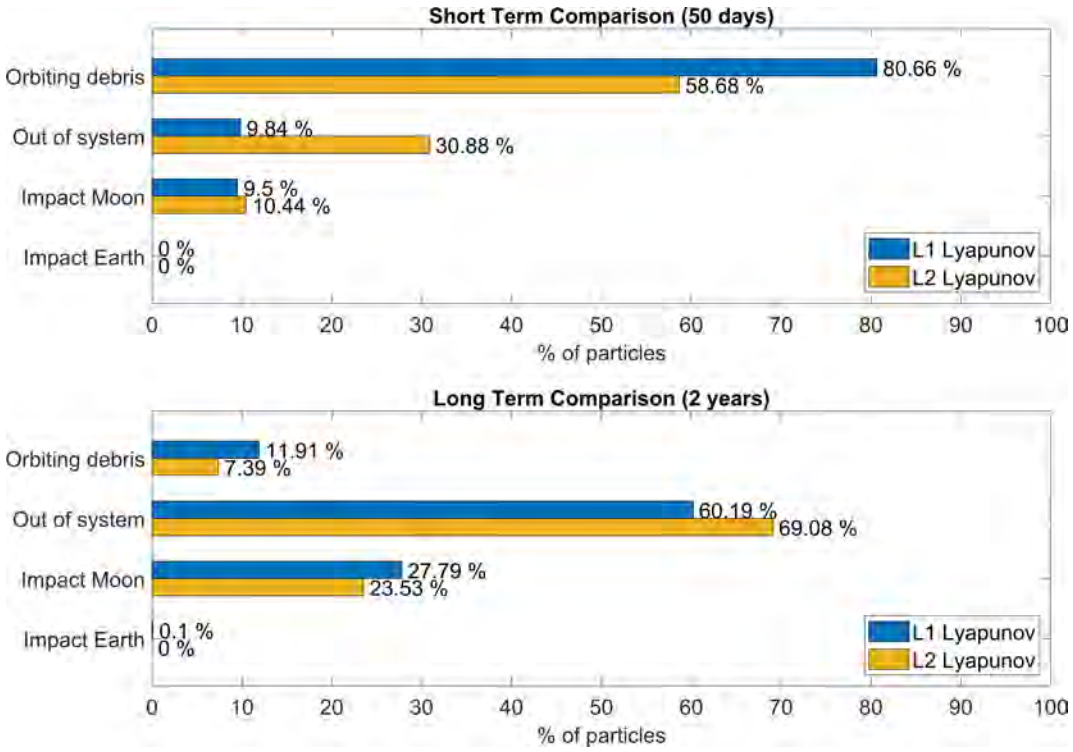

Figure 4.25 Debris evolution of explosions occurring in L_1 and L_2 Lyapunov orbits

To study other parameters in the system, some danger zones are defined as spherical volumes. In this study, danger zones are applied to the Libration Points L_1 and L_2, but they could be computed for other orbiting satellites as well as other points or objects of interest.

The danger zone is defined as a spherical region of a radius of $10,000$ km. When a fragment enters the region, it is considered that it has some probability of hitting the object which is applied to the danger zone [12]. The results of this study are plotted in Figure 4.26.

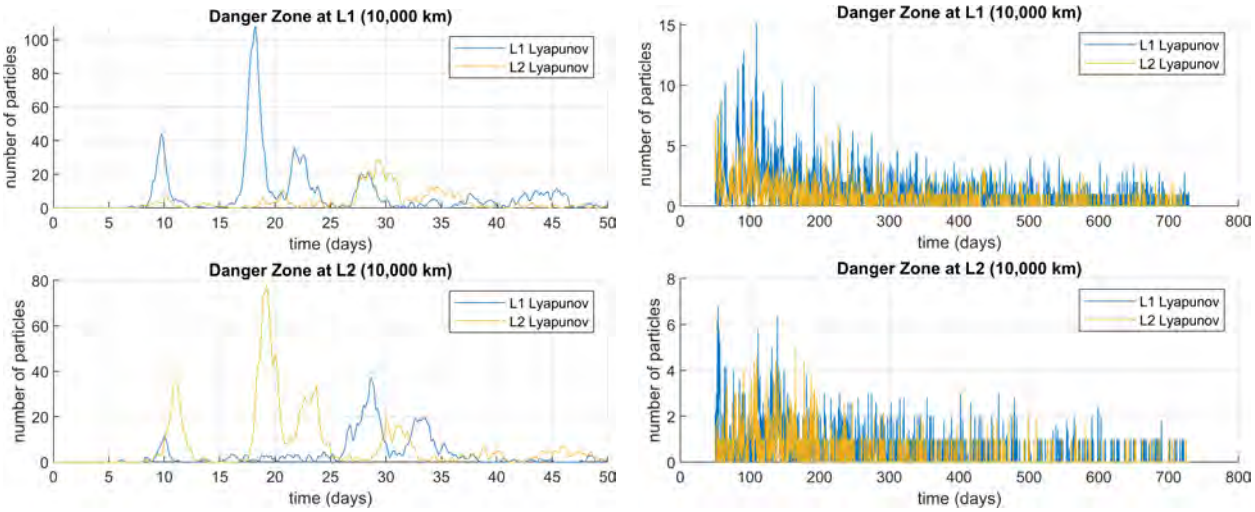

(a) Comparison for the Short Term

(b) Comparison for the Long Term

Figure 4.26 Number of particles inside the danger zone of L_1 and L_2 Libration Points

It is observed that there is a certain dependence on the initial position where the explosion takes place. Over the long term, no more than 15 fragments are inside these danger zones.

However, it is observed that in the short term, there are peaks with a larger number of fragments. The main peak occurs after almost 20 days, which corresponds approximately to 2 orbital periods. Some particles have already gone out of the initial path, but they have not been dragged out of the region yet.

The pattern described is valid for both cases, observing that the highest peak in the danger zone of L_1 corresponds to debris due to explosions in L_1 Lyapunov and in the same way for the case of L_2 and its Lyapunov orbits.

4.4 Distant Retrograde Orbits

A different simulation is computed for DROs, analyzing a greater number of explosions in this case. 200 spacecraft' outputs are compiled and analyzed along the initial orbit. All the explosions computed occur at the same time. This study is evaluated only for the short term, i.e., 50 days, because of the large number of fragments generated. Two animation snapshots are included in

Figure 4.27. Fragments tend to remain in the vicinity of the orbit path, particularly one week after the fragmentation events occur, as shown in Figure 4.27a. One month later, animation stills display the stability and relatively few particles leave the system, depicted in the developing ring in Figure 4.27b.

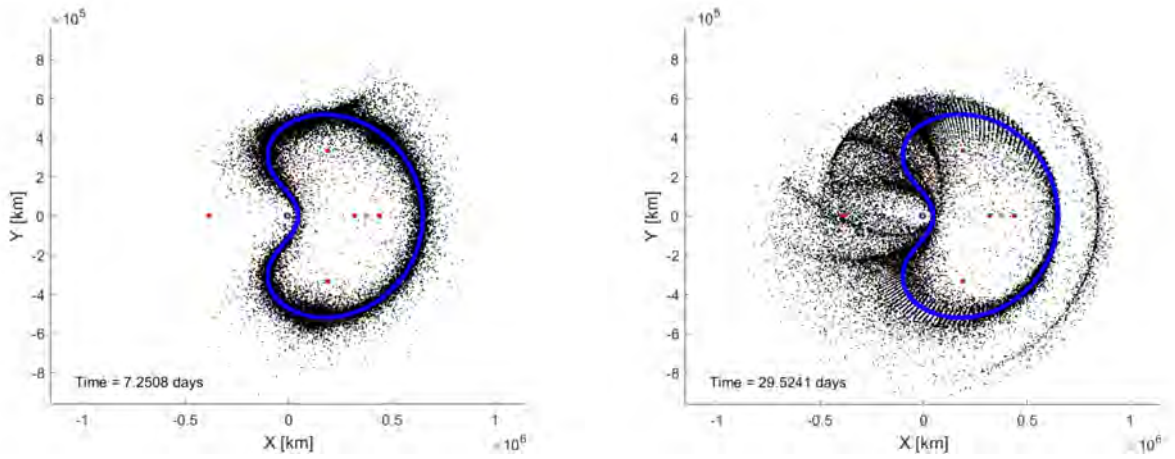

(a) One week *(b)* One month

Figure 4.27 Debris propagation from a DRO at different times

The resulting impact is largely upon future DRO missions as a result. The plots in Figure 4.28 correspond to spherical danger zones with a radius of 40,000 km about L_1, L_2, L_4, and L_5 respectively. Very few particles approach the Lagrange points over the 50-day span.

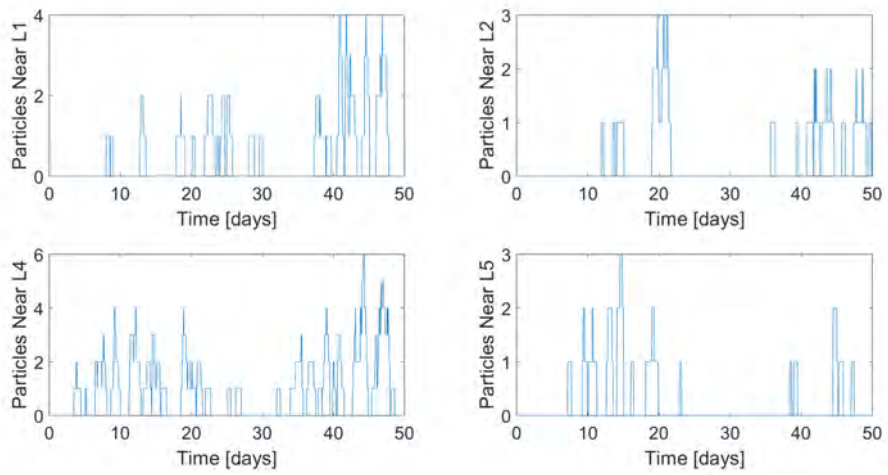

Figure 4.28 Count of particles in proximity to Lagrange points over time (DRO explosions)

4.5 Validation of results using a higher-fidelity ephemeris model

The results are now compared with a higher-fidelity ephemeris model to evaluate whether the debris evolution exhibits similar behavior observed as in the simulations obtained using the CR3BP. The higher fidelity model uses the SPICE libraries [29], provided by NASA's Navigation and Ancillary Information Facility (NAIF), to obtain positions and velocities of bodies of interest. The ephemeris model simulates the motion of an object relative to a central body of mass and it considers the perturbation of other bodies [23]. In this case, the motion of the fragments is modeled with the Earth as the central body while including other perturbing bodies such as the Moon and the Sun, positioned relative to Earth. The motion of the Moon is assumed to be on its plane within the CR3BP using the Ecliptic J2000.0 planet-centered reference inertial frame. The motion of the debris under study is defined by the acceleration obtained as:

$$\ddot{\bar{r}}_{E-obj} = \frac{-G(m_{obj}+m_E)}{r^3_{E-obj}}\bar{r}_{E-obj} + Gm_M\left(\frac{\bar{r}_{obj-M}}{r^3_{obj-M}} - \frac{\bar{r}_{E-M}}{r^3_{E-M}}\right) + Gm_S\left(\frac{\bar{r}_{obj-S}}{r^3_{obj-S}} - \frac{\bar{r}_{E-S}}{r^3_{E-S}}\right) \quad (44)$$

where m_{obj} is the mass of the debris object, which is neglected in this study, and each term of the equation represents the influence of the gravitational acceleration due to the central body, and the perturbing interactions of the Moon (subscript 'M') and the Sun (subscript 'S'). Note that the mutual interaction between debris particles is neglected due to their insignificant mass. One of the primary limitations of the ephemeris model is its dependency on epochs. To better compare the results with those obtained by applying the CR3BP, an initial epoch is selected where the distance between the Earth and the Moon matches the characteristic distance of the CR3BP. In this case, the epoch selected corresponds to April 28th, 2024 at 04:00:00 pm. The problem is non-dimensionalized by using the Earth-Moon instantaneous characteristic quantities at each time [30].

To validate the results obtained using the CR3BP, the scenario analyzed in Section 4.1, which involves simulating 40 explosions in a sample of five L_1 Lyapunov orbits, is computed using the aforementioned higher-fidelity ephemeris model for the propagation of the fragments. The first conclusion drawn is that the ephemeris model adds a significantly higher computational cost; computational time is considerably increased due to retrieving the SPICE information. This

observation supports the hypothesis that the CR3BP model is preferable for simulating large quantities of debris due to its computational efficiency. Figure 4.29 illustrates the evolution of debris over 2 years obtained using the ephemeris model. Compared to Figures 4.3a and 4.3b, the results illustrate that the short-term propagation is very similar in both cases, with more significant differences emerging after two years of simulation. However, these differences do not exceed 10%, as presented in Figure 4.30, indicating sufficient accuracy for the time of evolution selected in this study. The increasing discrepancies over time also confirm that the CR3BP model is less suitable for longer periods, as it lacks the precision of the ephemeris model. However, as the ephemeris model is also numerically integrated, precision decreases as propagation time increases. It is also important to consider that the ephemeris model accounts for the effect of the Sun and is highly dependent on the epoch, as previously noted. Therefore, the results are not identical at any point in the simulation.

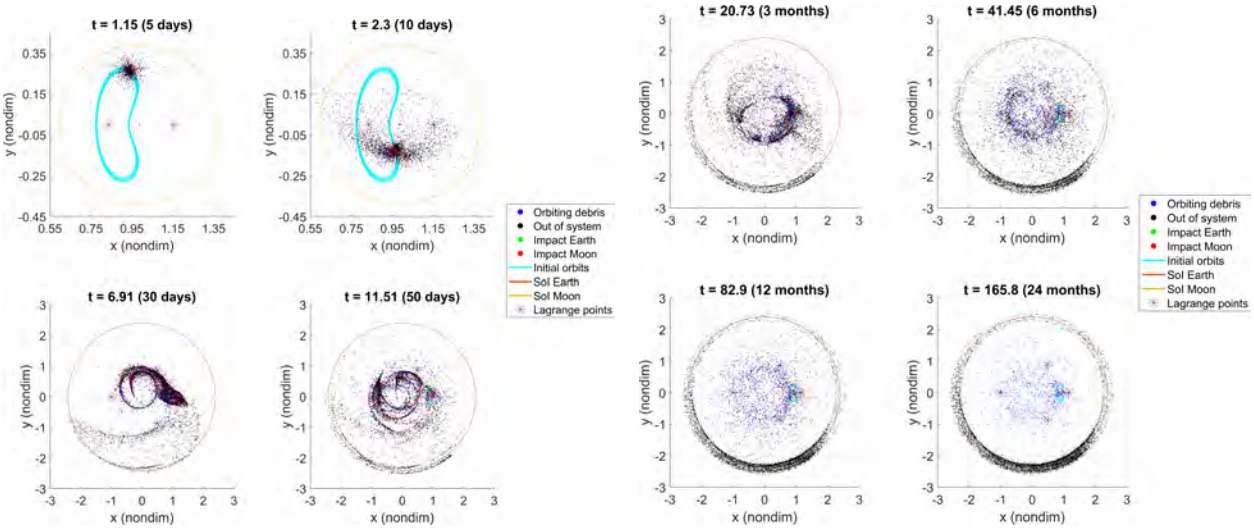

(a) Short Term *(b)* Long Term

Figure 4.29 Simulation over 2 years for explosions in L_1 Lyapunov orbits (Ephemeris Model)

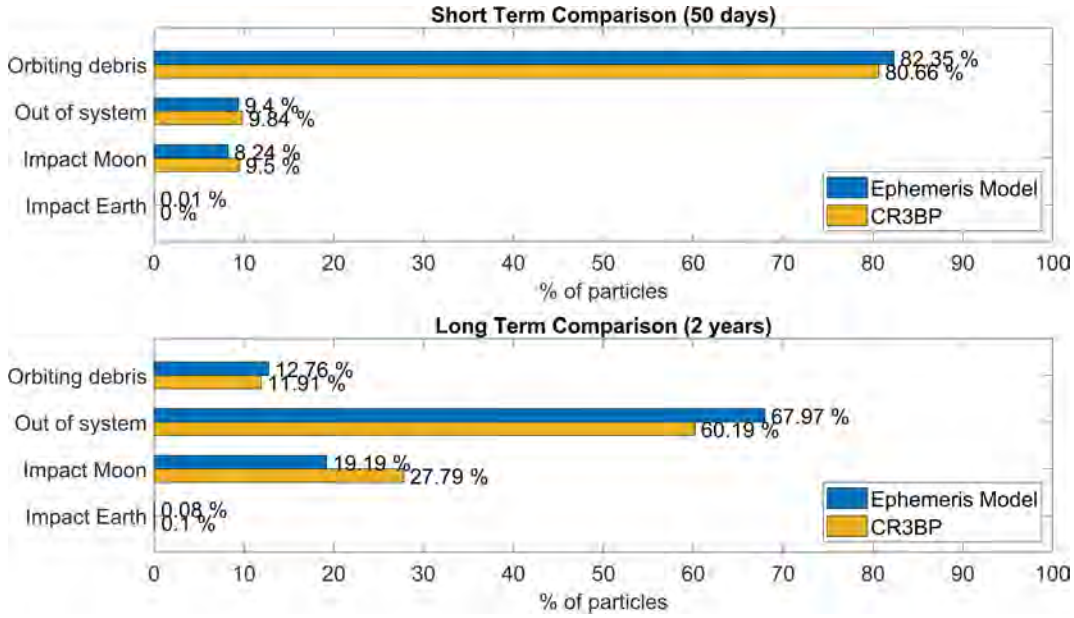

Figure 4.30 Debris evolutions of explosions applying the CR3BP and Ephemeris Model

5 Impact in other orbiting spacecraft

This section analyzes the effect of debris on a different satellite. There are some cases of study presented in this research: explosion at L_1 Lyapunov orbit, impact on the same family and L_2 Lyapunov orbit, and explosion at L_2 Lyapunov orbit, impact on that family and L_1 Lyapunov orbit.

5.1 Explosions at L_1 Lyapunov orbit

Firstly, the debris studied in Section 4.1 is analyzed assessing how it affects other satellites orbiting in the vicinity of the Moon. Satellites in two different orbits are selected: L_1 Lyapunov orbit with $JC = 3.0174$ and L_2 Lyapunov $JC = 3.0165$. Eight positions within each orbit are analyzed to examine the effect of the phase difference between the explosion points and the satellites affected by them.

5.1.1 Impact on L_1 Lyapunov orbit

Figure 5.1a shows the eight initial conditions of the satellites to be studied. These points are evenly spaced with respect to the orbital period. Figure 5.1b illustrates the position of each satellite at the time of the first explosion, as well as the location of the explosion, to observe their relative positions.

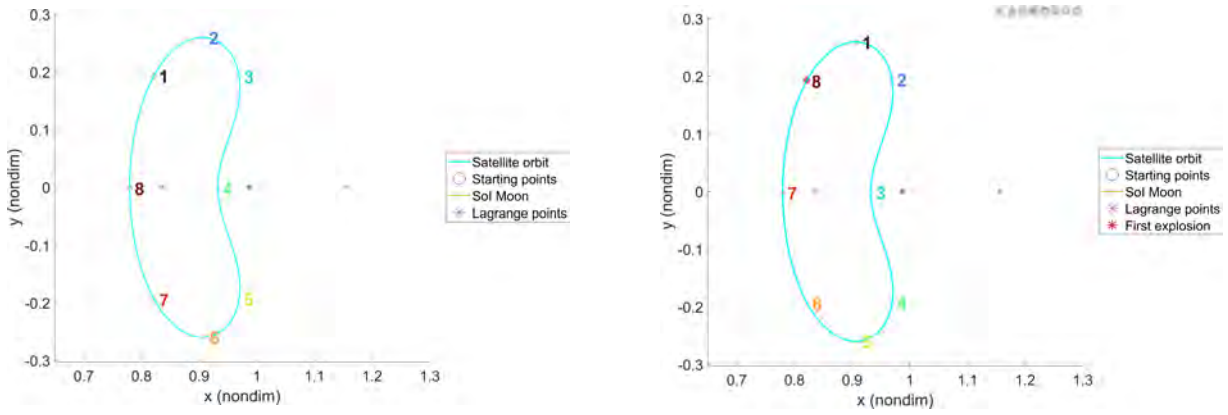

(a) IC of the orbiting s/c

(b) Position of each s/c during first explosion

Figure 5.1 Initial state of the system (L_1 Lyapunov explosions & L_1 Lyapunov s/c)

Plots analyzing the effect on satellite 8 are separated for more detailed analysis. As shown in Figure 5.1b, the explosion occurs very near this satellite, significantly increasing the risk it faces. Most of the observed events occur in the short term, so the following figures focus on the first 50

days. However, the final results obtained after the two-year simulation are also provided for a more comprehensive analysis.

To study the danger posed by explosions to satellites in orbit, the concept of danger zones defined in Section 4.3 is revisited. In most of the studied cases, two significant peaks are observed, with a higher number of particles entering the danger zone, as shown in Figure 5.2a. These peaks occur approximately 10 days apart, slightly less than the studied orbital period. The first peak shifts earlier and becomes smaller as the satellites are further ahead in their orbit relative to the explosions. However, the number of particles increases further ahead. In cases where explosions occur roughly at the same location as the satellite, a larger peak is observed each time an explosion occurs, as presented in Figure 5.2b.

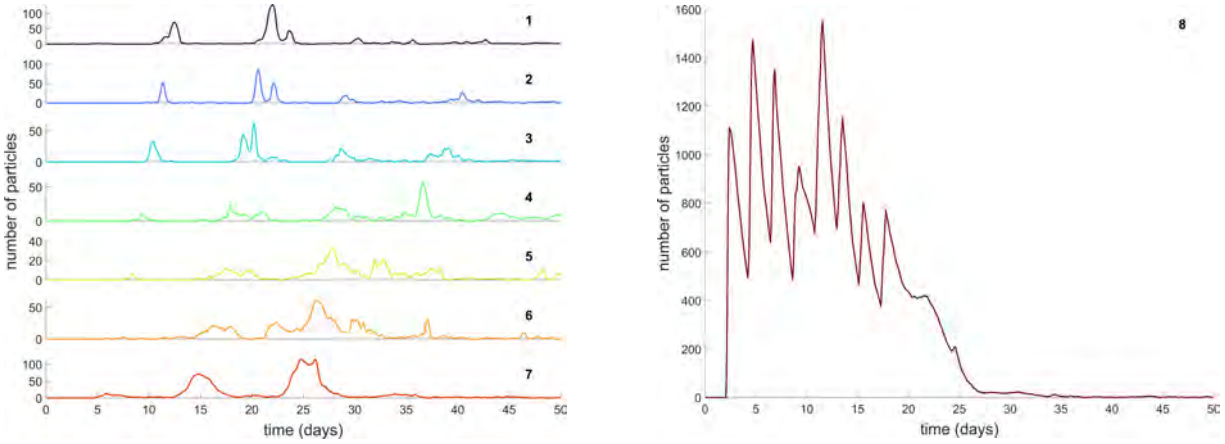

(a) Fragments in danger zone of s/c (1-7) *(b)* Fragments in danger zone of s/c 8

Figure 5.2 Short term evolution of L_1 Lyapunov s/c danger zones (L_1 Lyapunov explosions)

Although by looking at danger zones, it is possible to identify moments when the proximity of debris to satellites in orbit may create risky situations, it does not quantify that danger. To clarify this, the concept of *expected hits* [12] is introduced. It is assumed that when a particle enters a spherical zone, called the hazard zone, around the satellite, a potential impact is implied. The radius of this zone is defined as 500 m. Due to the expected low number of fragments within this zone and its small size, the tolerances of the problem and the simulation itself may result in no accurate outcomes. Therefore, the assumption is made that the distribution of particles within the danger zone is uniform. By calculating the ratio between the volumes of both spherical zones, i.e.,

$10,000^3/500^3$, the expected number of impacts is determined. Note that each particle is counted only once every time it enters the danger zone, regardless of the time it spends within this zone. Figure 5.3 shows the cumulative number of expected hits over time for each satellite. It is observed that most potential impacts occur within the first 15 to 30 days after the explosions, leading to a more stable situation thereafter.

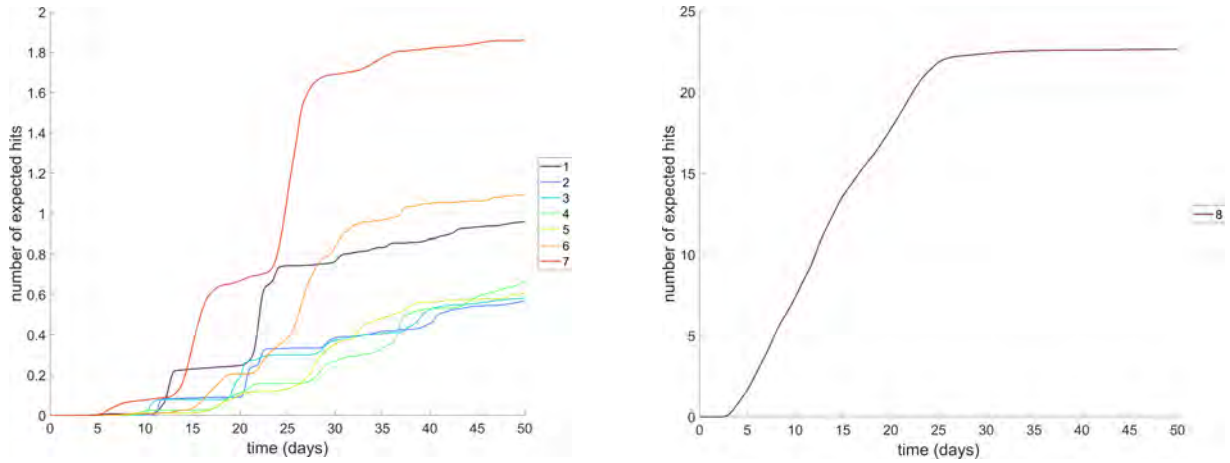

(a) Expected hits of s/c (1-7) *(b)* Expected hits of s/c 8

Figure 5.3 Short term expected hits of L_1 Lyapunov s/c (L_1 Lyapunov explosions)

The results after two years of simulation are presented in Table 5.1. It is observed that satellites 3-5, which have the greatest phase difference relative to the orbital position where explosions occur, have the lowest risk of being impacted. The results are based on the debris studied in Section 4.1, which considers the explosion of 40 different satellites.

Table 5.1 Expected hits for L_1 Lyapunov s/c over 2 years (L_1 Lyapunov explosions)

IC orbiting s/c	**Expected hits**
1	3.4734
2	3.3879
3	3.1330
4	2.9766
5	2.8890
6	3.5303
7	4.2901
8	24.9265

Considering this data, it appears that the studied satellites are at a high risk of being impacted. However, averaging across all initial positions and considering the explosion of a single satellite,

the expected number of hits reduces to 0.15. Although this number is significantly lower, it still represents a considerable risk.

5.1.2 Impact on L_2 Lyapunov orbit

Figure 5.4a illustrates the eight initial conditions of the satellites to be studied in this section. Figure 5.4b displays the relative position of these satellites to the point where debris is generated in this case. It also presents the initial orbit of the exploding satellites, allowing for the observation of interaction between both orbits.

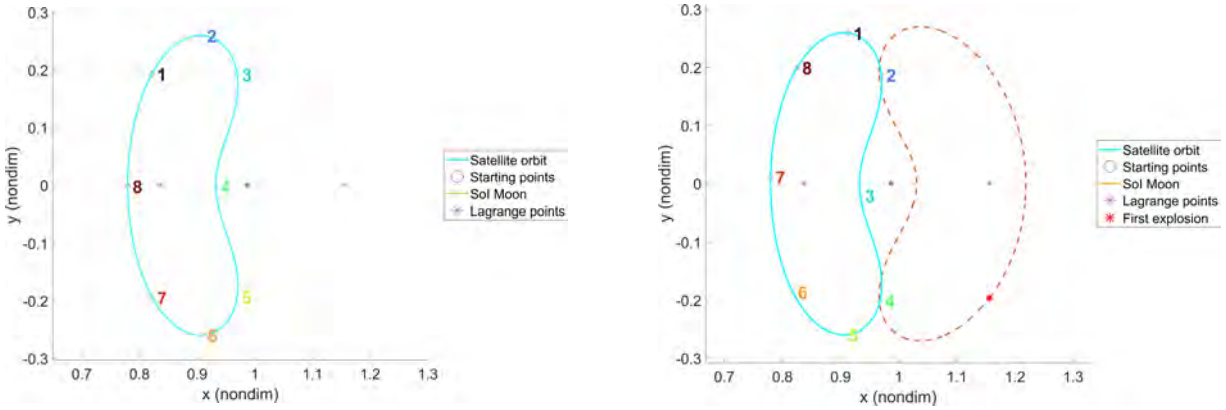

(a) IC of the orbiting s/c

(b) Position of each s/c during first explosion

Figure 5.4 Initial state of the system (L_1 Lyapunov explosions & L_2 Lyapunov s/c)

The evolution of the fragments regarding the satellites' danger zones is presented in Figure 5.5. Half of the observed satellites experience brief periods when the particle concentration within their respective danger zones is exceptionally high. To analyze this fact, these satellites are divided into two groups:

- First, satellites 1 and 2 have their closest lunar passage immediately after the start of the explosions. Therefore, they pass through the ring of debris generated around the Moon, as shown in Section 4.1.7. The next satellite to pass through this region is satellite 8, and it no longer encounters the debris cloud, which has already impacted the Moon.
- Second, attention is focused on satellites 5 and 6. These two satellites pass through the apoapsis of their orbits shortly after the explosion, the farthest region from the generated debris. From Section 4.1.5, it is inferred that the energy level of debris creates a funnel effect

for fragments heading toward Earth after the explosion. Although not in large numbers, they pass through a narrow passage that is also traversed by the satellites of study.

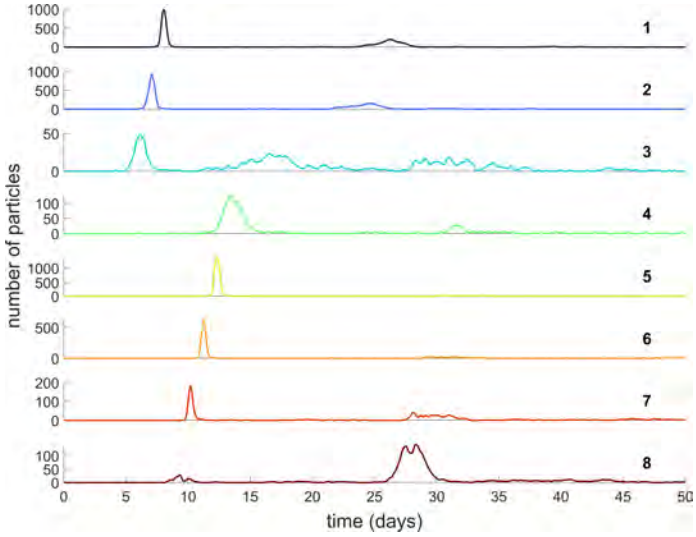

Figure 5.5 Short term evolution of L_2 Lyapunov s/c danger zones (L_1 Lyapunov explosions)

The effect of the aforementioned encounters is presented in Figure 5.6. However, it is observed that this effect is not as significant as expected. Due to their short duration, their impact on the risk experienced by the satellites is not as high as compared to interference from a smaller amount of debris but spread over a longer period.

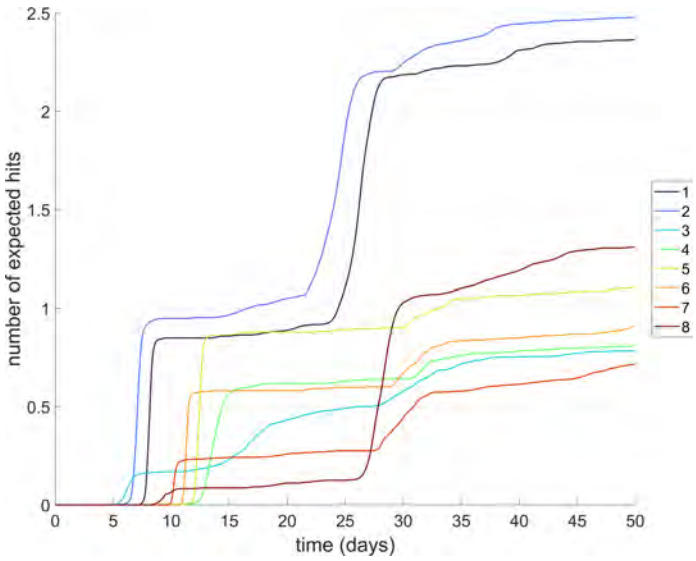

Figure 5.6 Short term expected hits of L_2 Lyapunov s/c (L_1 Lyapunov explosions)

The number of expected hits at the end of the simulation time is indicated in Table 5.2. It is confirmed that satellites closer to apoapsis, i.e., farthest from the initial explosions, experience the

least risk. To contextualize the data, considering an average of all satellites and assuming a single explosion, it is extrapolated that approximately 0.06 expected hits occur.

Table 5.2 Expected hits for L_2 Lyapunov s/c over 2 years (L_1 Lyapunov explosions)

IC orbiting s/c	Expected hits
1	3.5761
2	3.8196
3	2.0345
4	2.0978
5	2.4151
6	2.1851
7	1.9230
8	2.534

5.2 Explosions at L_2 Lyapunov orbit

In this section, the same study is applied using the debris assessed in Section 4.2. Eight positions within the L_1 Lyapunov orbit ($JC = 3.0174$) and the L_2 Lyapunov orbit ($JC = 3.0165$) are used as the initial conditions of the satellites analyzed for their safety after the explosions occur.

5.2.1 Impact on L_2 Lyapunov orbit

In this case, Figure 5.7a represents the initial positions of the eight satellites to be studied. The position of each satellite is also illustrated in Figure 5.7b at the moment of the first explosion, as well as the explosion's position, allowing for an appreciation of their relative positions. As in Section 5.1.1, satellite 8 is separated in subsequent plots for individual analysis.

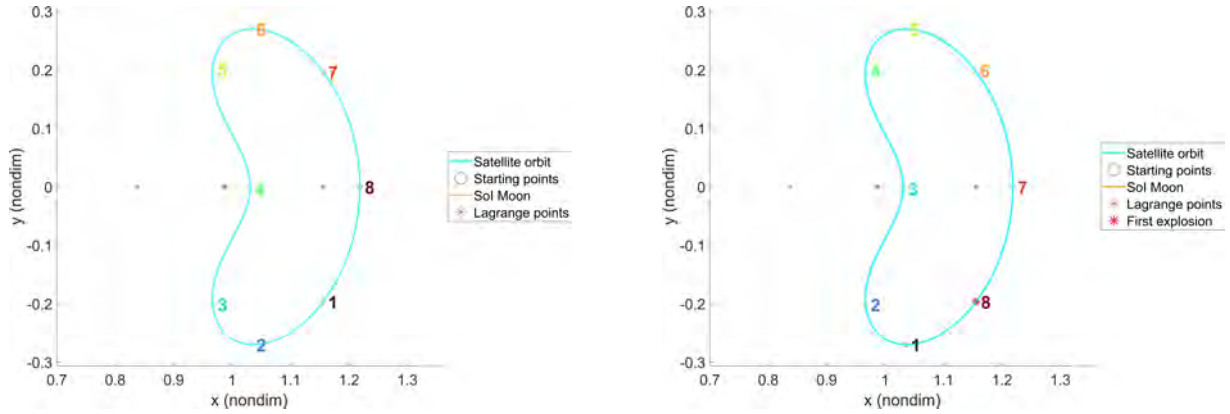

(a) IC of the orbiting s/c *(b)* Position of each s/c during first explosion

Figure 5.7 Initial state of the system (L_2 Lyapunov explosions & L_2 Lyapunov s/c)

Figure 5.8 displays the number of fragments within the danger zone, and the evolution of

the expected hits over time is presented in Figure 5.9. These plots reveal that their morphology is practically identical to those observed in Section 5.1.1, where it is analyzed the impact of explosions on observed satellites orbiting in the same orbit family.

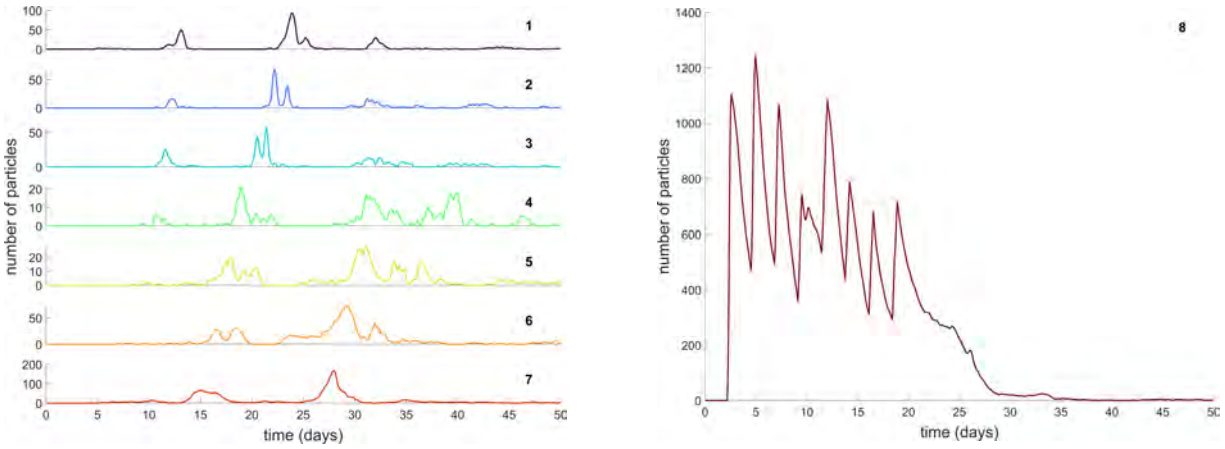

(a) Fragments in danger zone of s/c (1-7) *(b)* Fragments in danger zone of s/c 8

Figure 5.8 Short term evolution of L_2 Lyapunov s/c danger zones (L_2 Lyapunov explosions)

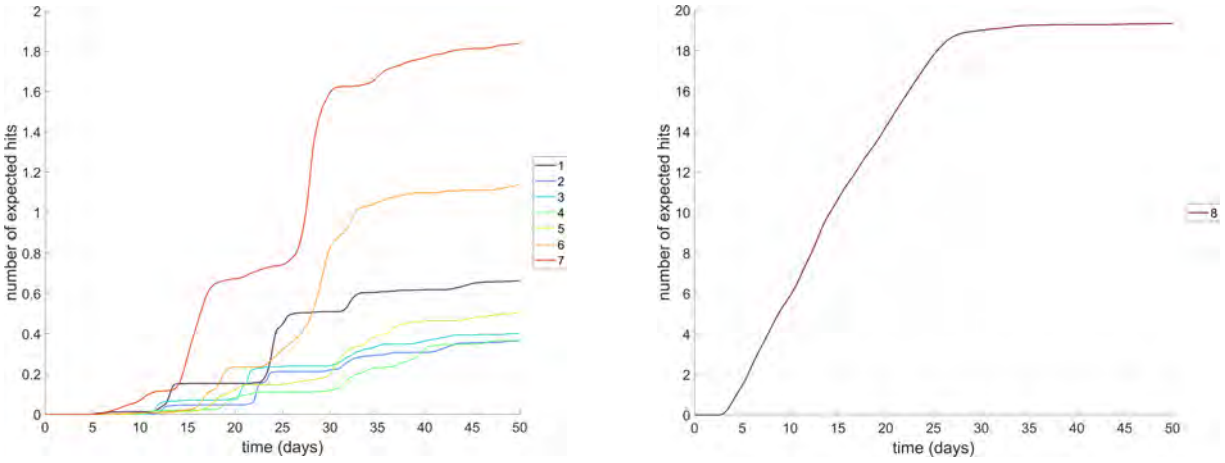

(a) Expected hits of s/c (1-7) *(b)* Expected hits of s/c 8

Figure 5.9 Short term expected hits of L_2 Lyapunov s/c (L_2 Lyapunov explosions)

To appreciate a distinction, it is necessary to consider the values in Table 5.1 and 5.3, noting that for L_2 Lyapunov orbits, the values are lower. This fact indicates a reduced risk of collision following the explosion. Using the same extrapolation, for a single satellite in a debris cloud generated by an explosion, it is obtained that there are 0.10 expected hits, which is $1/3$ less than in the case of L_1 Lyapunov case of study.

Table 5.3 Expected hits for L_2 Lyapunov s/c over 2 years (L_2 Lyapunov explosions)

IC orbiting s/c	Expected hits
1	1.7458
2	1.3925
3	1.4741
4	1.357
5	1.5816
6	2.2215
7	2.8132
8	20.3883

5.2.2 Impact on L_1 Lyapunov orbit

Figure 5.10a shows the eight initial conditions of the satellites to be studied in this section. Figure 5.10b displays the relative position of these satellites to the point and the initial orbit where the simulated explosions occur.

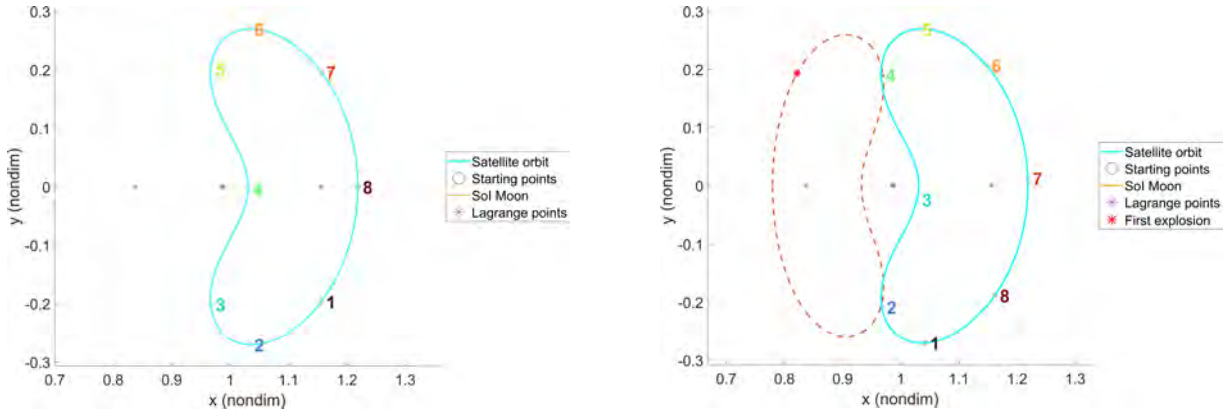

(a) IC of the orbiting s/c *(b)* Position of each s/c during first explosion

Figure 5.10 Initial state of the system (L_2 Lyapunov explosions & L_1 Lyapunov s/c)

When examining Figure 5.11 and comparing it with the one obtained in Section 5.1.2, it is observed that the highlighted events are completely analogous. The satellites with an equivalent initial relative position to the orbit where the explosions occur show identical peaks in debris encounters.

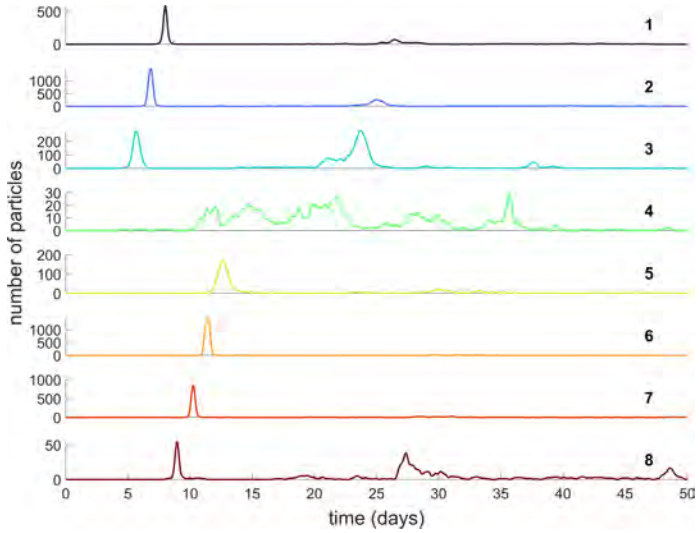

Figure 5.11 Short term evolution of L_1 Lyapunov s/c danger zones (L_2 Lyapunov explosions)

The patterns observed in Figure 5.12 regarding the number of expected hits are similarly compared to those observed in the study of the effect of explosions in L1 on satellites orbiting in L2 Lyapunov.

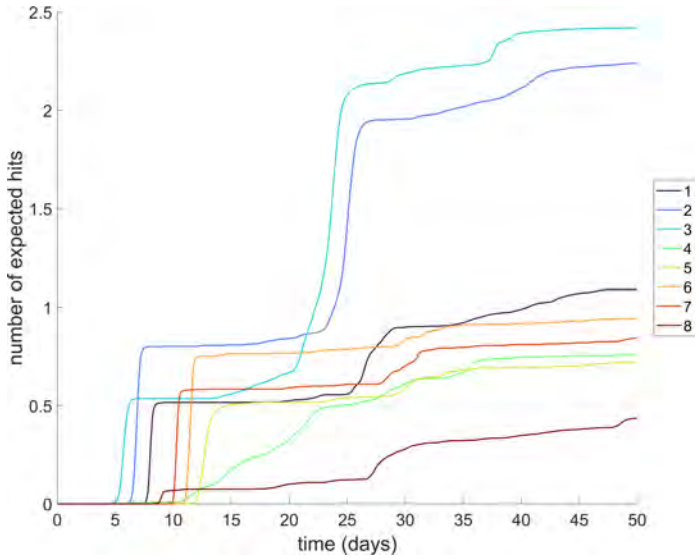

Figure 5.12 Short term expected hits of L_1 Lyapunov s/c (L_2 Lyapunov explosions)

The results after two years of simulation are presented in Table 5.4. In this case, assuming a single explosion and its effect on a singular satellite, it is found that the satellite would face 0.07 expected hits. This number is very similar and even slightly higher than the one obtained in Section 5.1.2 with which this case is compared.

Table 5.4 Expected hits for L_1 Lyapunov s/c over 2 years (L_2 Lyapunov explosions)

IC orbiting s/c	**Expected hits**
1	2.5509
2	3.5696
3	3.9516
4	2.2565
5	2.1601
6	2.4077
7	4.2715
8	1.8448

After analyzing each section individually and comparing them, the conclusion drawn is that satellites in closer proximity to the explosion positions face the highest risk of collision. This risk is also heightened for satellites passing through a region very near the Moon within a short time frame, typically a matter of days, especially when the explosion occurs near the periapsis of their orbit.

6 Conclusions and Future Work

This research represents a step ahead in the study of spacecraft fragmentation, a field of interest for the safety of future missions. Although debris analysis has been done previously, there are some gaps in the impact assessment, such as debris computation which leads to problems related to memory and time computation. These issues have been identified and solved by the creation of databases. By following the entire process for generating new databases, the computation may take around 20 minutes to 4 hours. It is possible to create different debris databases with a time investment of 5 minutes once the explosions are saved. By applying the new process, some results have been obtained and analyzed, leading to conclusions about the fragmentation events and confirming the chaotic behavior of the system.

Results confirm the effectiveness of the new process in the propagation of spacecraft fragments. This enhances computational efficiency and provides deeper insights into debris behavior and its implications for space safety. By propagating debris clouds, it is possible to assess the impact in the Cislunar region as well as the impact in other orbiting satellites.

While this research is focused on Lyapunov orbits, applying the same process to different orbit families will yield more conclusions regarding mission safety.

Future work in this research will help to understand and reduce the risks associated with fragmentation events in the Cislunar region. By applying the method to various initial conditions, such as considering other periodic orbit families, it will be possible to conclude the most hazardous scenarios and the impact of the orbiting explosion and the nearby missions.

Further progress in this study will help to draw new policies regarding the location of future missions. They may be determined based on how debris accumulates in different areas of interest. In the coming years, as technology continues to advance and the amount of space traffic in the Cislunar region increases, it will be important to establish regulations that minimize the likelihood of catastrophic events occurring between neighboring missions.

REFERENCES

[1] Guardabasso, P., and Lizy-Destrez, S., "Lunar Orbital Debris Mitigation: Characterisation of the Environment and Identification of Disposal Strategies," 2021.

[2] Baker-McEvilly, B., Doroba, S., Gilliam, A., Criscola, F., Canales, D., Frueh, C., and Henderson, T., "A review on hot-spot areas within the Cislunar region and upon the Moon surface, and methods to gather passive information from these regions," *AAS/AIAA 33rd Space Flight Mechanics Meeting*, 2023.

[3] Baker-McEvilly, B., Bhadauria, S., Canales, D., and Frueh, C., "A comprehensive review on Cislunar expansion and space domain awareness," *Progress in Aerospace Sciences*, Vol. 147, 2024, p. 101019. https://doi.org/https://doi.org/10.1016/j.paerosci.2024.101019, URL https://www.sciencedirect.com/science/article/pii/S0376042124000459.

[4] NASA, "Artemis Plan; NASA's Lunar Exploration Program Overview," 2020.

[5] Abell, P., Bailey, B., Beaty, D., and Beinhoff, D., "The Lunar Exploration Roadmap: Exploring the Moon in the 21st Century: Themes, Goals, Objectives, Investigations, and Priorities," *Lunar Exploration Analysis Group*, 2013.

[6] Letizia, F., Colombo, C., Lewis, H., and McInnes, C., "Debris cloud evolution in Low Earth Orbit," 2013.

[7] Landgraf, M., and Jehn, R., "Space Debris Hazards from Explosions in the collinear Sun-Earth Lagrange points," 2001.

[8] Davidson, J. R., *Environmental Problems of Space Flight Structures: II. Meteoroid Hazard*, National Aeronautics and Space Administration, 1963.

[9] Burbank, P. B., Cour-Palais, B. G., and Mc Allum, W. E., "A meteoroid environment for

near-earth, cislunar, and near-lunar operations," Tech. rep., 1965.

[10] Bettinger, R. A., Boone, N., Hamilton, N. S., and Little, B. D., "Spacecraft Charging Vulnerability near the Stable Earth-Moon Lagrange Points," *2021 IEEE Aerospace Conference (50100)*, 2021, pp. 1–9. https://doi.org/10.1109/AERO50100.2021.9438151.

[11] Slíz-Balogh, J., Barta, A., and Horváth, G., "Celestial mechanics and polarization optics of the Kordylewski dust cloud in the Earth–Moon Lagrange point L5 – I. Three-dimensional celestial mechanical modelling of dust cloud formation," *Monthly Notices of the Royal Astronomical Society*, Vol. 480, No. 4, 2018, pp. 5550–5559. https://doi.org/10.1093/mnras/sty2049.

[12] Boone, N., and Bettinger, R., "Debris Propagation Following a Spacecraft Mishap at the Collinear Earth-Moon Lagrange Points," 2021, pp. 1–15. https://doi.org/10.1109/AERO50100.2021.9438276.

[13] Wilmer, A. P., Boone, N. R., and Bettinger, R. A., "Artificial Debris Propagation in Cislunar Periodic Orbits," *2021 AAS/AIAA Astrodynamics Specialist Conference*, 2021.

[14] Boone, N. R., and Bettinger, R. A., "Spacecraft survivability in the natural debris environment near the stable Earth-Moon Lagrange points," *Advances in Space Research*, Vol. 67, No. 8, 2021, pp. 2319–2332.

[15] Boone, N., and Bettinger, R., "Artificial Debris Collision Risk Following a Catastrophic Spacecraft Mishap in Lunar Orbit," 2021.

[16] Bettinger, M. R., Boone, N., Hamilton, M. N., and Little, L. C. B., "Survivability Analysis in the Shadow of Apollo: Part II–Spacecraft Charging Vulnerability Near the Stable Earthmoon Lagrange Points," 2021.

[17] Boone, N., and Bettinger, R., "Long-Term Evolution of Debris Clouds in Low Lunar Orbit," 2022.

[18] Wilmer, A. P., Boone, N. R., and Bettinger, R. A., "Debris Propagation and Spacecraft Survivability Assessment for Catastrophic Mishaps Occurring in Cislunar Periodic Orbits," *The Journal of Space Safety Engineering*, Vol. 9, No. 2, 2022, pp. 207–222. https://doi.org/10.1016/j.jsse.2022.02.007.

[19] Black, A., and Frueh, C., "Characterizing Cislunar Fragmentations," *The Advanced Maui Optical and Space Surveillance Technologies Conference, Maui, HI*, 2023.

[20] Black, A., and Frueh, C., "Investigation of Fragmentation Events in the Cislunar Domain," *33rd AAS/AIAA Space Flight Mechanics Meeting, Austin, TX*, 2023.

[21] Vallado, D., and McClain, W., *Fundamentals of Astrodynamics and Applications*, Fundamentals of Astrodynamics and Applications, Microcosm Press, 2001.

[22] Curtis, H., *Orbital Mechanics: For Engineering Students*, Aerospace Engineering, Elsevier Science, 2015.

[23] Canales Garcia, D., "Transfer design methodology between neighborhoods of planetary moons in the circular restricted three-body problem," Ph.D. thesis, Purdue University, 12 2021. https://doi.org/10.25394/PGS.17147630.v1, URL https://hammer.purdue.edu/articles/thesis/Transfer_design_methodology_between_neighborhoods_of_planetary_moons_in_the_circular_restricted_three-body_problem/17147630.

[24] Frueh, C., Howell, K., DeMars, K. J., and Bhadauria, S., "Cislunar space situational awareness," *31st AIAA/AAS Space Flight Mechanics Meeting*, 2021, pp. 6–7.

[25] Johnson, N., Krisko, P., Liou, J.-C., and Anz-Meador, P., "NASA's new breakup model of evolve 4.0," *Advances in Space Research*, Vol. 28, 2001, pp. 1377–1384. https://doi.org/10.1016/S0273-1177(01)00423-9.

[26] SpaceFlight 101, "NOAA 16 Satellite Breakup Leaves Dozens of

Debris in Orbit," , Dec. 2019. URL https://spaceflight101.com/noaa-16-satellite-breakup-leaves-dozens-of-debris-in-orbit/.

[27] Wilmer, A. P., "Space Domain Awareness Assessment of Cislunar Periodic Orbits for Lagrange Point Surveillance," Tech. rep., AIR FORCE INSTITUTE OF TECHNOLOGY WRIGHT-PATTERSON AFB OH, 2021.

[28] Liou, J.-C., "Orbital Debris and Future Environment Remediation," Presentation, 2012.

[29] Acton, C., Bachman, N., Semenov, B., and Wright, E., "A look towards the future in the handling of space science mission geometry," *Planetary and Space Science*, Vol. 150, 2018, pp. 9–12. https://doi.org/https://doi.org/10.1016/j.pss.2017.02.013.

[30] Anderson, A., McCann, B., Canales, D., and Nazari, M., "Utilizing the geometric mechanics framework to predict attitude in a full ephemeris model of the Cislunar region," *Communications in Nonlinear Science and Numerical Simulation*, Vol. 130, 2023, p. 107726. https://doi.org/DOI:10.1016/j.cnsns.2023.107726.